ARTICLES
https://doi.org/10.1038/s41594-021-00646-x

nature structural & molecular biology

Cryo-EM structures of hIAPP fibrils seeded by patient-extracted fibrils reveal new polymorphs and conserved fibril cores

Qin Cao[1,3], David R. Boyer[1], Michael R. Sawaya[1], Romany Abskharon[1], Lorena Saelices[1,4], Binh A. Nguyen[1,4], Jiahui Lu[1], Kevin A. Murray[1], Fouad Kandeel[2] and David S. Eisenberg[1]✉

Amyloidosis of human islet amyloid polypeptide (hIAPP) is a pathological hallmark of type II diabetes (T2D), an epidemic afflicting nearly 10% of the world's population. To visualize disease-relevant hIAPP fibrils, we extracted amyloid fibrils from islet cells of a T2D donor and amplified their quantity by seeding synthetic hIAPP. Cryo-EM studies revealed four fibril polymorphic atomic structures. Their resemblance to four unseeded hIAPP fibrils varies from nearly identical (TW3) to non-existent (TW2). The diverse repertoire of hIAPP polymorphs appears to arise from three distinct protofilament cores entwined in different combinations. The structural distinctiveness of TW1, TW2 and TW4 suggests they may be faithful replications of the pathogenic seeds. If so, the structures determined here provide the most direct view yet of hIAPP amyloid fibrils formed during T2D.

The tissue deposition of amyloid fibrils is a hallmark of the amyloid family of diseases, including Alzheimer's disease, Parkinson's disease and type II diabetes (T2D). These fibrils are associated with and possibly causal of disease[1]. Associated with T2D are fibrils of hIAPP (or amylin), a human protein hormone of 37 residues, which works with insulin to regulate blood sugar levels[2,3]. Pancreatic amyloid deposits of hIAPP are found in more than 90% of T2D patients[4–6], and genetic and experimental evidence links them to the pathogenic mechanism of T2D[7–11]. Accordingly, determining the near-atomic-resolution structures of these disease-related hIAPP fibrils may help to understand the molecular mechanism of pathogenesis of T2D, and can offer essential information for the structure-based design of inhibitors of amyloidosis.

Our previous cryo-EM study revealed the structure of amyloid fibrils formed by full-length recombinant hIAPP fused to a small ubiquitin-like modifier (SUMO)-tag[12], adding to the collection of models and near-atomic-resolution structures reported for fibrils of synthetic and untagged hIAPP peptide[13–16]. Whereas these structures were all obtained from hIAPP fibrils formed in vitro, recent studies on tau and α-synuclein suggest that in vitro fibrils may not adopt the same structures as patient-extracted fibrils[17,18]. These findings raise the question of whether the reported hIAPP fibril structures are disease-related. In this Article, we extract hIAPP fibrils from islet cells of a donor with T2D to seed the fibril formation of synthetic hIAPP, and determine four cryo-EM structures from seeded fibrils, with the expectation that the seeded fibrils may replicate the structure of the seeds (Supplementary Text 1).

Results

T2D patient fibrils seed fibrilization of synthetic hIAPP. We extracted hIAPP fibrils from the islet cells of a donor with T2D, and used these extracted fibrils to seed the fibril formation of synthetic hIAPP peptides. We first tested the amyloid content in islet cells from seven donors with T2D (donors 1 to 7) by Congo red staining. Samples from one donor (donor 6) exhibited strong Congo red staining while samples from two other donors (donors 4 and 5) exhibited medium staining (Fig. 1a, Extended Data Fig. 1a and Supplementary Table 1). We selected donor 6 for further study. Genotyping revealed that the hIAPP encoded was wild type. We then performed fibril extraction from islet cells of donor 6 by following the protocol reported previously and combined with immunoprecipitation (Methods). Our goal was to determine the structure of T2D-relevant hIAPP fibrils. However, patient extracted fibrils are too scarce for cryo-EM study. To amplify the quantity of sample, we used patient-extracted fibrils to seed synthetic hIAPP, generating abundant, long fibrils for cryo-EM determination (Fig. 1 and Extended Data Fig. 1; for details see Methods).

Cryo-electron microscopy structures of seeded hIAPP fibrils. We identified eight different morphologies during two-dimensional (2D) classification: four were clearly twisted (termed TW1–4) and suitable for structure determination and four were not twisted (termed NT1–4; Fig. 2 and Extended Data Fig. 2a,b). TW1 is the most abundant species and contains ~30% of all identifiable segments, whereas TW2, TW3 and TW4 contain 15%, 10% and 10%, respectively. NT1–4 together account for the remaining 35% of particles, but their lack of twisting precludes 3D structure determination. We determined the cryo-EM structures of TW1 to TW4 with resolution ranging from 3.8 to 4.1 Å (Fig. 2, Extended Data Figs. 2c–e and 3 and Table 1). These structures displayed the typical cross-β scaffold of amyloid fibrils, consisting of layers of β-strands stacked with 4.8-Å spacing (Fig. 2 and Extended Data Fig. 3).

[1]Departments of Chemistry and Biochemistry and Biological Chemistry, UCLA-DOE Institute, Molecular Biology Institute, and Howard Hughes Medical Institute, UCLA, Los Angeles, CA, USA. [2]Department of Translational Research & Cellular Therapeutics, City of Hope, Duarte, CA, USA. [3]Present address: Bio-X Institutes, Key Laboratory for the Genetics of Developmental and Neuropsychiatric Disorders, Ministry of Education, Shanghai Jiao Tong University, Shanghai, China. [4]Present address: Center for Alzheimer's and Neurodegenerative Diseases, Department of Biophysics, UT Southwestern Medical Center, Dallas, TX, USA. ✉e-mail: david@mbi.ucla.edu

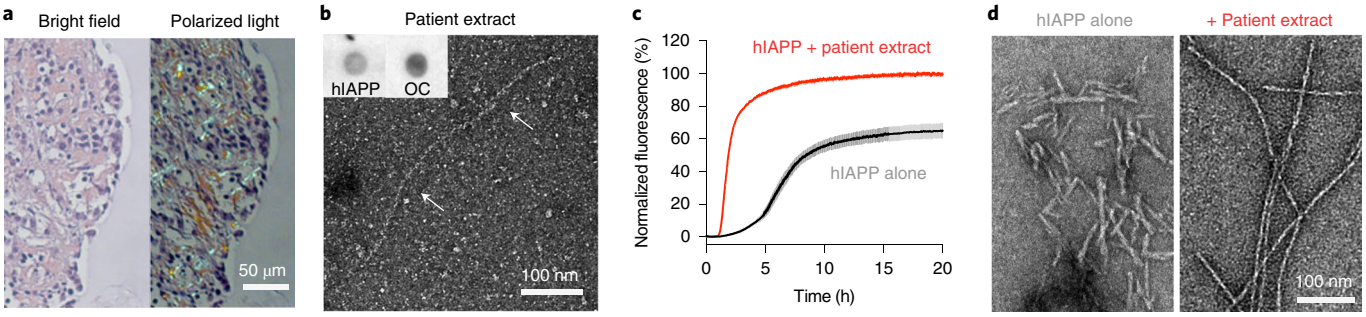

Fig. 1 | Extraction of patient islet cells and seeding of fibril growth. a, Congo red staining of a slice of islet cells from a donor with T2D (donor 6). **b**, Negatively stained EM image of the elute-1 fraction in the immunoprecipitation assay. Amyloid fibrils are indicated by arrows. Insets: dot blots of the same fraction probed by anti-hIAPP (amylin polyclonal antibody) and anti-amyloid fibril OC antibodies. **c**, ThT aggregation curves of freshly prepared synthetic hIAPP peptide incubated with (red) and without (black) the patient extracted fibrils as fibril growth seeds. Data are shown as mean ± s.d., $n = 3$ independent experiments. **d**, Negatively stained EM images of the same samples as in **c** after 20 h of incubation.

All four fibril polymorphs are composed of two intertwined chains or protofilaments. The two protofilaments are related by a C_2 symmetry axis in the TW2 fibrils and by a pseudo-$P2_1$ axis in TW3 fibrils. In TW1 and TW4, which we term heterotypic fibrils, the two protofilaments (chains A and B) are conformationally distinct from each other (Fig. 2 and Extended Data Fig. 4a).

We note that at the current resolution (3.7 to 4.1 Å), cryo-EM refinement usually suffers from local minima problems[19], which may raise the risk of an incorrect map and/or model. However, we were able to build unambiguous models based on map fitting as well as external information, such as cross-validation via other structures and determining the terminus of the main chain (see Methods for details).

In the final models, we observed density for the C-terminal residue of hIAPP (Tyr37) in all chains except for TW4 chain B (Extended Data Fig. 5a). The lack of additional density beyond Tyr37 in all polymorphs except TW4 chain B and the lack of space for building additional residues beyond Tyr37 in TW2, TW3 and TW4 chain A supports the registration of the models into the maps (Extended Data Figs. 2c and 5b,c). Furthermore, the finding that the amide moiety of Tyr37 forms a hydrogen bond to stabilize the fibril fold on TW2, TW3 and TW4 chain A is consistent with the previous observation that C-terminal amidation promotes amyloidosis of hIAPP[20] (Extended Data Fig. 5c). Density for the N-terminal region was more variable; the first ordered residue differs among polymorphs from Thr6 (in TW2 and TW4 chain A) to Val17 (TW1 chain B; Extended Data Fig. 5a). In TW2–4, we found extra density near the N terminus, suggesting the position of additional N-terminal residues (Fig. 2, Extended Data Fig. 5b and Discussion).

Three seeded polymorphs are previously unreported forms. Three of the four seeded hIAPP fibril structures are distinct from previously reported unseeded ones. We consider fibrils 6Y1A[15] and 6ZRF[16] as the unseeded controls of our study, given that, in all three studies, identical starting material (C-terminally amidated hIAPP) and similar fibril growth conditions were used. Those two unseeded control studies revealed fibril structures similar to each other (disregarding the opposite assignment of fibril handedness, Extended Data Fig. 4b; see Methods for details) as the dominant species (90% and 80% of total fibril populations, respectively). In our seeded experiment, we found that one species, TW3, matches the dominant conformation of 6Y1A and 6ZRF (Extended Data Fig. 4b), but it contributes only 10% of the total population. The majority of the seeded fibrils are polymorphs TW1, TW2 and TW4, whose structures differ from the unseeded controls.

Structural alignment at the protofilament level. We selected all unique hIAPP conformations (a single layer in a protofilament in a fibril) among all reported hIAPP fibril structures (Table 2) and performed pairwise structural alignment (Methods and Supplementary Table 2). We found all conformations except TW2 can be categorized into two groups: core fold 1 (CF1) and core fold 2 (CF2; Fig. 3a,b, Supplementary Text 2 and Extended Data Fig. 6). Unlike the other structures, TW2 is composed of unique protofilament folds, as evidenced by the superposition with TW1 chain A and chain B (Extended Data Fig. 4d). In the following, we refer to the fold of TW2 as core fold 3 (CF3).

CF1 and CF2 form different protofilament interfaces. The two core folds (CF1, CF2) we observe in most hIAPP fibril structures can be combined in three different ways to form a fibril. All three have been observed, including the two homotypic types, CF1-CF1 (TW1, 6Y1A and 6ZRF) and CF2-CF2 (6ZRR, 6ZRQ and 6VW2), and the heterotypic type, CF1-CF2 (TW1, TW4 and 6ZRR; Fig. 3b). The interfaces at which the different protofilaments meet are not conserved; for example, when aligned at CF2 (chain B of TW1, TW4 and 6ZRR), we found that the other chains from these three structures are not aligned (Fig. 3c). We examined all substantial interfaces of protofilaments presented in hIAPP fibril structures (Extended Data Fig. 5f), and we found all these interfaces are different (Supplementary Text 3), suggesting that polymorphism arises at the level of protofilament assembly into fibrils.

Comparison of wild-type and S20G hIAPP fibril structures. S20G of hIAPP is the only hereditary mutation found so far in T2D patients, and it has been reported to increase the amyloidosis of hIAPP and cause early onset of T2D[21–24]. Structures of hIAPP fibrils containing the S20G mutation have been determined and deposited in the PDB with codes 6ZRR and 6ZRQ[16]. By contrast, the genotype of the patient sample of our study identifies the seeds as wild-type hIAPP, and the seeded synthetic monomeric hIAPP we used is also wild type. Comparison of the S20G structures with the wild-type structures reveals that S20G structures exhibit the same conserved kernels, CF1 and CF2, as the wild-type structures (Fig. 3b). These observations suggest that the S20G mutation enhances fibrilization not by creating new core folds, but instead by favoring the same folds exhibited by wild-type hIAPP.

To improve our understanding of the mechanism by which S20G stabilizes hIAPP fibril structures, we marked position 20 on hIAPP structures with arrows (Fig. 3b) and found that all are located at or near sharp kinks in the main chain. Because the glycine residue is more permissive of a kinked conformation, we suggest that the

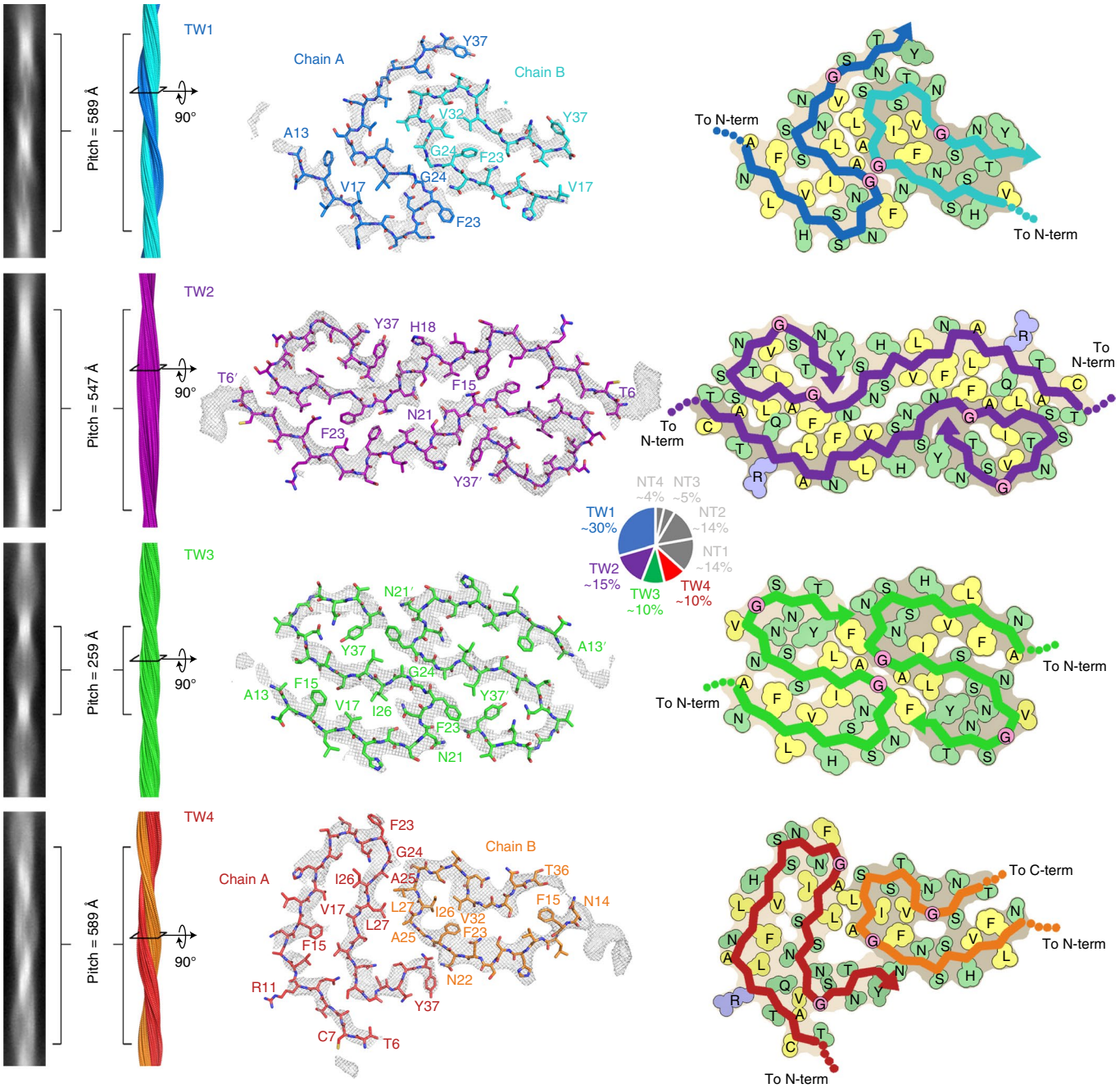

Fig. 2 | Cryo-EM structures of patient extract-seeded hIAPP fibrils. Far left: representative 2D classes of four morphologies that display twisting features (TW1–TW4). Middle left: fibril reconstructions of TW1–TW4 scaled to match the 2D classes. The pitch of each morphology is labeled. Middle right: density and atomic model of one cross-sectional layer of each morphology. The asterisk marks residual density that may represent an unknown ligand (also see Extended Data Fig. 5d). Far right: schematic model of each morphology. Hydrophobic residues are shown in yellow, polar ones in green, glycines in pink and arginines in blue. N-term, N terminus; C-term, C terminus. The percentages of total helical segments belonging to each morphology are shown in the pie chart in the middle, and the numbers are calculated via 2D classification.

S20G hereditary mutation promotes amyloid formation by allowing the peptide chain to more easily adopt a fibril-forming fold.

In addition to favoring a kinked conformation in the main chain, we found another mechanism by which S20G may favor CF2 over CF1 and CF3. We found that among all hIAPP protofilaments that contain CF2, the backbone phi angle at position 20 is positive, whereas the phi angle of position 20 in all other protofilaments is negative (Fig. 3d). Positive phi angles are favored by glycine more than any of the other 19 amino acid residues, because only glycine lacks a side chain larger than hydrogen that would otherwise clash with the main chain in this conformation. This observation suggests that S20G relieves the steric clash among protofilaments that contain CF2, permitting their formation. This hypothesis is supported by the observation that protofilaments with CF2 are more abundant in the S20G fibril dataset than in wild-type datasets, with the exception of 6VW2 (Extended Data Fig. 7a). We note in the 6VW2 dataset that the fibrils are formed by SUMO-tagged recombinant hIAPP without C-terminal amidation, differing from the synthetic and untagged hIAPP used in the studies of 6Y1A, 6ZRR and 6ZRQ[15,16]. So perhaps the existence of the SUMO-tag and/or the

Table 1 | Cryo-EM data collection, refinement and validation statistics

	TW1 (EMD-23686, PDB 7M61)	TW2 (EMD-23687, PDB 7M62)	TW3 (EMD-23688, PDB 7M64)	TW4 (EMD-23689, PDB 7M65)
Data collection and processing				
Magnification	×64,000	×64,000	×64,000	×64,000
Voltage (kV)	300	300	300	300
Electron exposure (e^-/Å^2)	45–85	45–85	45–85	45–85
Defocus range (μm)	0.7–2.7	0.7–2.7	0.7–2.7	0.7–2.7
Pixel size (Å)	1.055	1.055	1.055	1.055
Symmetry imposed	C_1	C_2	C_1	C_1
Helical rise (Å)	4.81	4.80	2.40	4.81
Helical twist (°)	−2.94	178.42	178.33	−2.94
Initial particle images (no.)	339,132	953,276	285,645	170,541
Final particle images (no.)	26,608	23,957	17,853	20,365
Map resolution (Å)	3.8	3.9	4.0	4.1
FSC threshold	0.143	0.143	0.143	0.143
Map resolution range (Å)	200–3.8	200–3.9	200–4.0	200–4.1
Refinement				
Initial model used (PDB code)	De novo	De novo	6Y1A	De novo
Model resolution (Å)	3.7	4.1	4.0	4.0
FSC threshold	0.5	0.5	0.5	0.5
Model resolution range (Å)	200–3.7	200–4.1	200–4.0	200–4.0
Map sharpening *B* factor (Å^2)	83	98	155	100
Model composition				
Nonhydrogen atoms	1,690	2,380	1,850	2,025
Protein residues	230	320	250	275
Ligands	0	0	0	0
B factors (Å^2)				
Protein	45.8	150.3	67.7	92.4
Ligand	-	-	-	-
R.m.s. deviations				
Bond lengths (Å)	0.007	0.007	0.008	0.009
Bond angles (°)	1.166	1.126	1.150	1.506
Validation				
MolProbity score	2.51	2.78	2.30	2.70
Clashscore	23.6	32.8	19.5	31.1
Poor rotamers (%)	0	0	0	0
Ramachandran plot				
Favored (%)	85.71	76.67	91.3	82.35
Allowed (%)	14.29	23.33	8.7	17.65
Disallowed (%)	0	0	0	0

lack of C-terminal amidation drives the fibrils in 6VW2 to the S20G favored CF2 conformation.

Structural similarity of hIAPP and amyloid-β fibrils. A clinical link between T2D and Alzheimer's disease has been reported[25–27], and evidence suggests that this link arises from the cross-seeding between hIAPP and amyloid-β fibrils in patients[28–32]. Cross-seeding is hypothesized to depend on the structural similarity between fibrils of hIAPP and amyloid-β. Previous structural comparisons between hIAPP and amyloid-β fibrils have supported this hypothesis[12,15,16]. Here, we perform comparisons while taking special note of the conserved core folds (CF1 and CF2). These cores, CF1 (residues 15–28) and CF2 (residues 20–33), each cover the region of maximal sequence similarity between hIAPP (19–29) and amyloid-β (24–34) (Fig. 3e), raising the question of whether analogous structural cores also exist in amyloid-β. We use TW1 chain A and chain B to represent protofilaments with CF1 and CF2, respectively, and, together with TW2 (CF3), we compare them with all available amyloid-β fibril structures. We confined our superpositions to the residue ranges exhibiting maximal sequence identity as noted above (Supplementary Table 3; see Methods for details). The comparisons reveal that each hIAPP core fold exhibits a root mean square deviation (r.m.s.d.) under 1.8 Å with some amyloid-β fibril structure. The best amyloid-β

Table 2 | Comparative solvation energy calculations

Fibril structure	Fibril information	Energy per layer (kcal mol^{-1})	Energy per residue (kcal mol^{-1})
TW1 (PDB 7M61)	Synthetic wild-type hIAPP peptide seeded by patient extract	−24.4	−0.53 (chain A, −0.58; chain B, −0.48)
TW2 (PDB 7M62)	Synthetic wild-type hIAPP peptide seeded by patient extract	−31.5	−0.49
TW3 (PDB 7M64)	Synthetic wild-type hIAPP peptide seeded by patient extract	−27.0	−0.54
TW4 (PDB 7M65)	Synthetic wild-type hIAPP peptide seeded by patient extract	−26.7	−0.49 (chain A, −0.49; chain B, −0.48)
6Y1A	Synthetic wild-type hIAPP peptide aggregated in vitro	−23.2	−0.46
6VW2	SUMO-tagged recombinant hIAPP aggregated in vitro	−21.6	−0.45
6ZRF	Synthetic wild-type hIAPP peptide aggregated in vitro	−24.0	−0.48
6ZRQ	Synthetic hIAPP S20G peptide aggregated in vitro	−25.1	−0.55
6ZRR	Synthetic hIAPP S20G peptide aggregated in vitro	−37.1	−0.54 (chain A, −0.53; chain B, −0.62; chain C, −0.46)

matches for each of the three groups of hIAPP protofilaments are as follows: 6OIZ with TW1 chain A, 2M4J with TW1 chain B and 5OQV and 6SHS with TW2 (Fig. 3e). These results suggest that hIAPP and amyloid-β may be able to cross-seed each other through these regions of sequence and structural similarity.

Discussion

Do our hIAPP structures recapitulate T2D patient seeds? In this study, we have determined the cryo-EM structures of four hIAPP polymorphs from fibrils seeded by patient-extracted seeds. Our structure TW3 is similar to 6Y1A[15] and 6ZRF[16] from unseeded controls. Structures TW1, TW2 and TW4 have not been reported before. Do these three seeding-specific polymorphs represent the presently unknown conformations of patient-extracted seeds, that is, of pathogenic hIAPP fibrils (Supplementary Text 4)?

A warning that seeded structures do not always replicate the structures of the seeds comes from a recent seeding study by Lövestam and colleagues[33]. Their work suggests that fibrils of recombinant α-synuclein seeded by patient extracts do not inevitably replicate the structures of the seeds[33]. In this α-synuclein study, two parallel seeding attempts using different patient extracted seeds generated seeded fibrils, whose structures were then determined. The structures were composed of two types of protofilament that were either essentially identical or close to that found in unseeded recombinant α-synuclein fibrils. However, a third parallel seeding attempt generated fibrils that largely replicated one out of two protofilaments of the seeds[33]. We believe these results suggest that there is a risk in seeding where the seeded protein may form fibrils that adopt the unseeded conformation, even in the presence of seeds. The third attempt by Lövestam et al. demonstrated that the structure of the seeds from the daughter fibrils can be obtained, at least at the level of the core fold of the protofilament. This emphasizes the importance of comparing the seeded fibril structures with unseeded controls at the protofilament level to judge which protofilament may represent the conformation of the seeds.

When we investigate the three new polymorphs found only in seeded hIAPP fibrils (TW1, TW2 and TW4) at the protofilament level, we find that TW2 adopts a unique conformation (CF3). We thus believe that CF3 is the most likely conformation to represent the seeds. By contrast, TW1 and TW4 both contain CF1 and CF2, which also exist in other unseeded hIAPP fibrils. We think this finding does not diminish the possibility that the structures of TW1 and TW4 are inherited from pathogenic hIAPP fibrils. Our reason is that, although TW1 and TW4 both contain a protofilament with CF1 that has been observed in the unseeded controls 6Y1A[15] and 6ZRF[16], TW1 and TW4 differ from these unseeded controls in that they also contain a protofilament with CF2. Therefore, the protofilaments that adopt CF2 can be considered as structural elements derived from the pathogenic seeds. We note that CF2 is also found in other unseeded hIAPP fibrils when either S20G (in 6ZRR and 6ZRQ[16]) or SUMO-tagged (in 6VW2[12]) hIAPP is used as the starting monomer. Therefore, we believe that CF2 can be adopted either through seeding with pathogenic fibrils or by changing the form of hIAPP used for unseeded fibril growth.

Additional factors may mitigate concern about the seeding fidelity in the present study. First, Lövestam et al. suggest that their failure to replicate structures via seeding may be due to the truncation and post-translational modification (PTM) of pathogenic α-synuclein fibrils[33]. These PTMs include ubiquitination and phosphorylation and are considered to favor α-synuclein fibril formation in patients, as does C-terminal truncation[34,35]. Apparently, when recombinant α-synuclein without PTMs or truncation is used for seeding, the daughter fibrils do not adopt the same structure as the seeds. However, PTMs other than the C-terminal amidation, which is present in our hIAPP monomer, or truncation are not required for hIAPP amyloidosis[36]. Furthermore, in contrast to previously determined, unseeded hIAPP fibril structures that mostly contain the C-terminal portion of hIAPP in the fibril core with the first visible residue around 13–15 (Extended Data Fig. 5a), residues 6–12 are visible in TW2 and chain A of TW4 and adopt similar conformations in both structures (Extended Data Fig. 5b, inset). The conformation of residues 1–5 is also indicated by weak densities in TW2 and chain A of TW4 (Extended Data Fig. 5b). The observation of the longer cores in TW2 and TW4 may also support their potential pathological origin, because in vivo fibril formation is much slower that in vitro, which will give the N terminus enough time to occupy a definite conformation. This hypothesis is further supported by the observation that α-synuclein fibrils extracted from patients' brains have larger ordered fibril cores than fibrils formed in vitro[18]. In short, the lack of sequence modifications, as well as larger ordered fibril cores may both suggest better fidelity of seeded replication of the hIAPP structure. In addition, hIAPP amyloid is linked with β-cell damage in T2D[37,38], and the observation that our seeded hIAPP fibrils are toxic to pancreas cells (Extended Data Fig. 9b) may add to the potential physiological relevance of this study.

We note that if our structures indeed replicate the conformations of pathogenic hIAPP fibrils, these fibrils are extracted from only one T2D patient. Although fibrils formed by the same protein and formed in different patients with the same disease were shown to adopt the same structures in tau and α-synuclein studies[18,39–41], it is still unknown if this is so for hIAPP fibrils in T2D. Further study with multiple patient samples is needed to address this question.

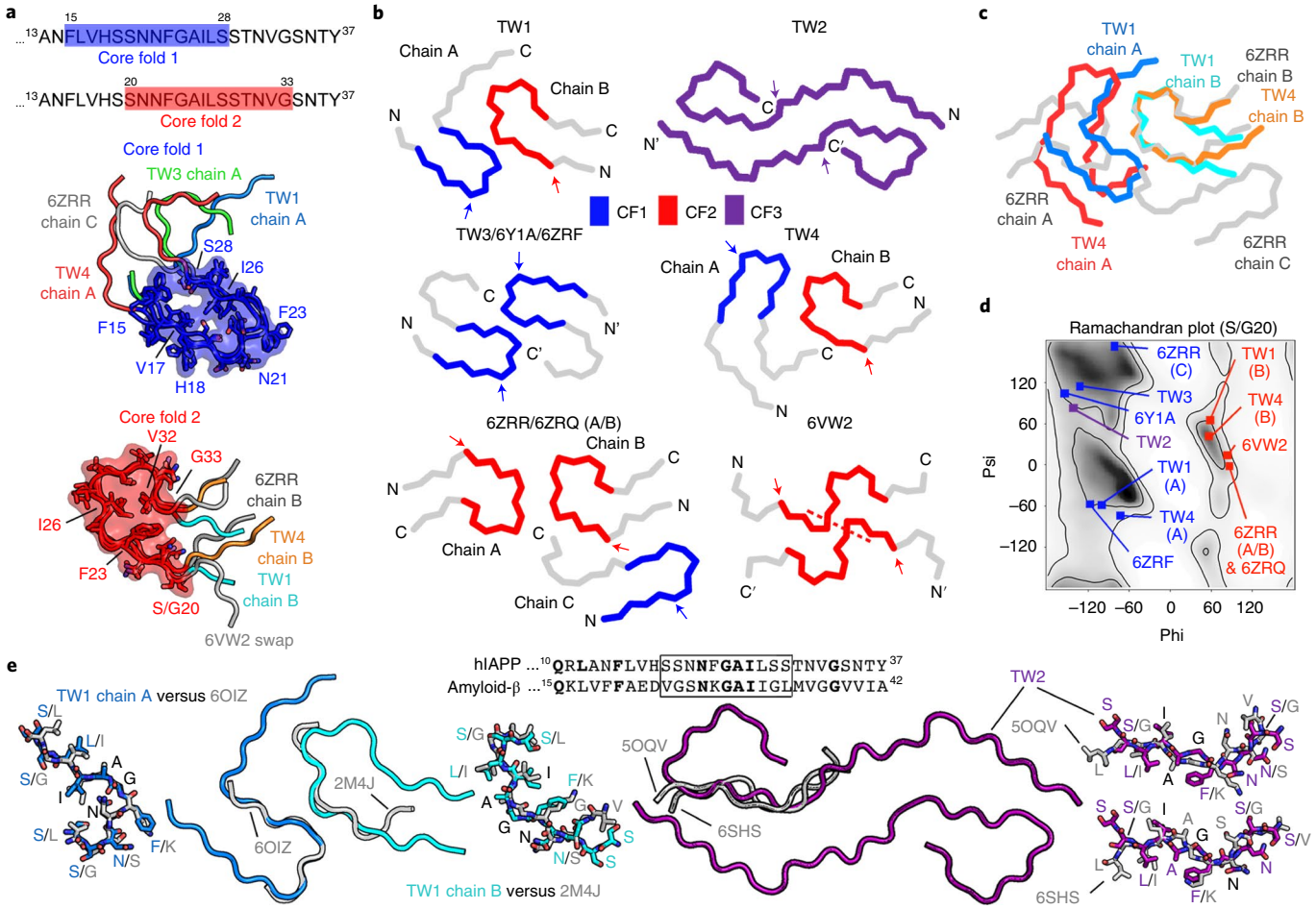

Fig. 3 | Structural comparisons of hIAPP fibrils seeded with patient-extracted fibrils. a, Two conserved core folds (CF1 and CF2) in the reported hIAPP fibril structures. Top: sequences of CF1 and CF2. Bottom: superposition of hIAPP fibril folds that contain CF1 and CF2. **b**, The six main chain views down the fibril axes of selected hIAPP structures. CF1, CF2 and CF3 are shown in blue, red and purple, respectively, and the rest of the main chains are gray. The arrows indicate the position of Ser20/Gly20. **c**, Superposition of TW1, TW4 and 6ZRR aligned on their CF2 regions of chain B. **d**, Ramachandran plot of position 20 of each hIAPP fibril structure, color coded for CF1 (blue), CF2 (red) and CF3 (purple). **e**, Structural alignments of TW1 (chain A, marine; chain B, cyan) and TW2 (purple) versus amyloid-β fibril structures (gray, residues 24–34 are shown). Inset: sequence alignment of hIAPP and amyloid-β. The boxed regions are predicted to be responsible for cross-seeding, and the residues that are identical in hIAPP and amyloid-β are shown in bold. For details of the superimposition of **a** and **e**, see Supplementary Table 2.

The origin of heterotypic pairings of hIAPP conformations. A notable finding in this study is that two distinct conformations of protofilaments pair together in two of our fibrils, TW1 and TW4 (Figs. 2 and 3b, Extended Data Fig. 4a, Supplementary Text 5 and Extended Data Fig. 8. Amyloid fibril structures with two protofilaments of different conformation have been reported several times (for example, recombinant H50Q α-synuclein fibrils[42] and brain extracted α-synuclein fibrils[18]), but the difference in conformation between protofilaments has never been as large as we observe in TW1 and TW4 in this study and 6ZRR from synthetic S20G hIAPP[16]. We think these unique fibrils combining different conformations are the result of hIAPP's propensity to adopt different core folds, and the ability of these different conformations to interface via different surfaces (Extended Data Fig. 5f).

Conclusion

In summary, in this study we have seeded fibril formation of synthetic hIAPP monomers with fibrils extracted from islet cells of a T2D patient and determined four cryo-EM structures of the seeded fibrils. Analysis of these structures and comparison with previously reported hIAPP fibril structures suggest the structural elements (CF3 and heterotypic assembly of CF1 and CF2) that are related to pathogenic hIAPP fibrils. Comparisons of wild type to S20G hIAPP fibril structures as well as hIAPP to amyloid-β fibril structures reveal the possible mechanism of how the hereditary mutation S20G facilitates hIAPP fibrilization in T2D and the regions that may enable hIAPP and amyloid-β cross-seeding.

Online content

Any methods, additional references, Nature Research reporting summaries, source data, extended data, supplementary information, acknowledgements, peer review information; details of author contributions and competing interests; and statements of data and code availability are available at https://doi.org/10.1038/s41594-021-00646-x.

Received: 9 April 2021; Accepted: 20 July 2021;
Published online: 9 September 2021

References

1. Eisenberg, D. & Jucker, M. The amyloid state of proteins in human diseases. *Cell* **148**, 1188–1203 (2012).
2. Roberts, A. N. et al. Molecular and functional characterization of amylin, a peptide associated with type 2 diabetes mellitus. *Proc. Natl Acad. Sci. USA* **86**, 9662–9666 (1989).

3. Westermark, P. Amyloid in the islets of Langerhans: thoughts and some historical aspects. *Ups. J. Med. Sci.* **116**, 81–89 (2011).
4. Westermark, P. et al. Amyloid fibrils in human insulinoma and islets of Langerhans of the diabetic cat are derived from a neuropeptide-like protein also present in normal islet cells. *Proc. Natl Acad. Sci. USA* **84**, 3881–3885 (1987).
5. Cooper, G. J. et al. Amylin found in amyloid deposits in human type 2 diabetes mellitus may be a hormone that regulates glycogen metabolism in skeletal muscle. *Proc. Natl Acad. Sci. USA* **85**, 7763–7766 (1988).
6. Höppener, J. W., Ahrén, B. & Lips, C. J. Islet amyloid and type 2 diabetes mellitus. *N. Engl. J. Med.* **343**, 411–419 (2000).
7. Westermark, P., Wernstedt, C., Wilander, E. & Sletten, K. A novel peptide in the calcitonin gene related peptide family as an amyloid fibril protein in the endocrine pancreas. *Biochem. Biophys. Res. Commun.* **140**, 827–831 (1986).
8. Westermark, G. T., Gebre-Medhin, S., Steiner, D. F. & Westermark, P. Islet amyloid development in a mouse strain lacking endogenous islet amyloid polypeptide (IAPP) but expressing human IAPP. *Mol. Med.* **6**, 998–1007 (2000).
9. Fernández-Alvarez, J. et al. Stable and functional regeneration of pancreatic β-cell population in nSTZ-rats treated with tungstate. *Diabetologia* **47**, 470–477 (2004).
10. Pilkington, E. H. et al. Pancreatic β-cell membrane fluidity and toxicity induced by human islet amyloid polypeptide species. *Sci. Rep.* **6**, 21274 (2016).
11. Mukherjee, A. et al. Induction of IAPP amyloid deposition and associated diabetic abnormalities by a prion-like mechanism. *J. Exp. Med.* **214**, 2591–2610 (2017).
12. Cao, Q., Boyer, D. R., Sawaya, M. R., Ge, P. & Eisenberg, D. S. Cryo-EM structure and inhibitor design of human IAPP (amylin) fibrils. *Nat. Struct. Mol. Biol.* **27**, 653–659 (2020).
13. Luca, S., Yau, W.-M., Leapman, R. & Tycko, R. Peptide conformation and supramolecular organization in amylin fibrils: constraints from solid-state NMR. *Biochemistry* **46**, 13505–13522 (2007).
14. Bedrood, S. et al. Fibril structure of human islet amyloid polypeptide. *J. Biol. Chem.* **287**, 5235–5241 (2012).
15. Röder, C. et al. Cryo-EM structure of islet amyloid polypeptide fibrils reveals similarities with amyloid-β fibrils. *Nat. Struct. Mol. Biol.* **27**, 660–667 (2020).
16. Gallardo, R. et al. Fibril structures of diabetes-related amylin variants reveal a basis for surface-templated assembly. *Nat. Struct. Mol. Biol.* **27**, 1048–1056 (2020).
17. Zhang, W. et al. Heparin-induced tau filaments are polymorphic and differ from those in Alzheimer's and Pick's diseases. *eLife* **8**, e43584 (2019).
18. Schweighauser, M. et al. Structures of α-synuclein filaments from multiple system atrophy. *Nature* **585**, 464–469 (2020).
19. Scheres, S. H. W. Amyloid structure determination in RELION-3.1. *Acta Crystallogr. D Struct. Biol.* **76**, 94–101 (2020).
20. Chen, M.-S. et al. Characterizing the assembly behaviors of human amylin: a perspective derived from C-terminal variants. *Chem. Commun.* **49**, 1799–1801 (2013).
21. Sakagashira, S. et al. Missense mutation of amylin gene (S20G) in Japanese NIDDM patients. *Diabetes* **45**, 1279–1281 (1996).
22. Meier, D. T. et al. The S20G substitution in hIAPP is more amyloidogenic and cytotoxic than wild-type hIAPP in mouse islets. *Diabetologia* **59**, 2166–2171 (2016).
23. Sakagashira, S. et al. S20G mutant amylin exhibits increased in vitro amyloidogenicity and increased intracellular cytotoxicity compared to wild-type amylin. *Am. J. Pathol.* **157**, 2101–2109 (2000).
24. Cao, P. et al. Sensitivity of amyloid formation by human islet amyloid polypeptide to mutations at residue 20. *J. Mol. Biol.* **421**, 282–295 (2012).
25. Janson, J. et al. Increased risk of type 2 diabetes in Alzheimer disease. *Diabetes* **53**, 474–481 (2004).
26. Miklossy, J. et al. Beta amyloid and hyperphosphorylated tau deposits in the pancreas in type 2 diabetes. *Neurobiol. Aging* **31**, 1503–1515 (2010).
27. Peila, R., Rodriguez, B. L., Launer, L. J. & Honolulu-Asia Aging Study. Type 2 diabetes, APOE gene, and the risk for dementia and related pathologies: The Honolulu-Asia Aging Study. *Diabetes* **51**, 1256–1262 (2002).
28. Oskarsson, M. E. et al. In vivo seeding and cross-seeding of localized amyloidosis: a molecular link between type 2 diabetes and Alzheimer disease. *Am. J. Pathol.* **185**, 834–846 (2015).
29. Moreno-Gonzalez, I. et al. Molecular interaction between type 2 diabetes and Alzheimer's disease through cross-seeding of protein misfolding. *Mol. Psychiatry* **22**, 1327–1334 (2017).
30. O'Nuallain, B., Williams, A. D., Westermark, P. & Wetzel, R. Seeding specificity in amyloid growth induced by heterologous fibrils. *J. Biol. Chem.* **279**, 17490–17499 (2004).
31. Krotee, P. et al. Common fibrillar spines of amyloid-β and human islet amyloid polypeptide revealed by microelectron diffraction and structure-based inhibitors. *J. Biol. Chem.* **293**, 2888–2902 (2018).
32. Andreetto, E. et al. A hot-segment-based approach for the design of cross-amyloid interaction surface mimics as inhibitors of amyloid self-assembly. *Angew. Chem. Int. Ed.* **54**, 13095–13100 (2015).
33. Lövestam, S. et al. Seeded assembly in vitro does not replicate the structures of α-synuclein filaments from multiple system atrophy. *FEBS Open Bio* **11**, 999–1013 (2021).
34. Fujiwara, H. et al. α-Synuclein is phosphorylated in synucleinopathy lesions. *Nat. Cell Biol.* **4**, 160–164 (2002).
35. Sorrentino, Z. A. & Giasson, B. I. The emerging role of α-synuclein truncation in aggregation and disease. *J. Biol. Chem.* **295**, 10224–10244 (2020).
36. Asthana, S., Mallick, B., Alexandrescu, A. T. & Jha, S. IAPP in type II diabetes: basic research on structure, molecular interactions and disease mechanisms suggests potential intervention strategies. *Biochim. Biophys. Acta Biomembr.* **1860**, 1765–1782 (2018).
37. Jurgens, C. A. et al. β-cell loss and β-cell apoptosis in human type 2 diabetes are related to islet amyloid deposition. *Am. J. Pathol.* **178**, 2632–2640 (2011).
38. Krotee, P. et al. Atomic structures of fibrillar segments of hIAPP suggest tightly mated β-sheets are important for cytotoxicity. *eLife* **6**, e19273 (2017).
39. Falcon, B. et al. Tau filaments from multiple cases of sporadic and inherited Alzheimer's disease adopt a common fold. *Acta Neuropathol.* **136**, 699–708 (2018).
40. Falcon, B. et al. Novel tau filament fold in chronic traumatic encephalopathy encloses hydrophobic molecules. *Nature* **568**, 420–423 (2019).
41. Zhang, W. et al. Novel tau filament fold in corticobasal degeneration. *Nature* **580**, 283–287 (2020).
42. Boyer, D. R. et al. Structures of fibrils formed by α-synuclein hereditary disease mutant H50Q reveal new polymorphs. *Nat. Struct. Mol. Biol.* **26**, 1044–1052 (2019).

Methods

Islet cells from donors with T2D. Islet cells from seven donors with T2D were provided by City of Hope as formalin-fixed paraffin-embedded slices to test the existence of amyloid deposits by Congo red staining. The basic information about each donor is listed in Supplementary Table 1. After Congo red staining, we selected the donor with the highest staining signal (donor 6), and frozen islet cells from this donor were further requested from City of Hope and used for genotyping and fibril extractions.

Congo red staining of fixed patient slices. Formalin-fixed paraffin-embedded slices of islet cells (thickness of 5 µm) were baked at 45 °C for 20 min for deparaffinization. The slices were then soaked three times in xylene (Fisher Scientific) for 5 min, then washed with 100%, 95%, 70% and 50% ethanol for 4 min, 4 min, 2 min and 2 min, respectively. The washed slices were soaked in water for 10 min on a shaker. The slices were Congo-red-stained using an amyloid stain, Congo red kit (Sigma-Aldrich), following the kit instructions. After Congo red staining, the slices were dipped twice in hematoxylin (Thermo Scientific) and rinsed in water for counter staining. After staining, the slices were washed three times with 100% ethanol for 5 min, rinsed in xylene, mounted with Permount mounting medium (Fisher Scientific) and allowed to dry for several hours. Stained slices were imaged by an AXIO Observer D1 fluorescence microscope (Zeiss) using bright-field and polarized light.

Genotyping of donor 6 hIAPP. To identify the genotype of the hIAPP from donor 6, we extracted genome DNA from the islet cells using the following protocol. Frozen islet cells were resuspended with 400 µl of SNET buffer (20 mM Tris pH 8.0, 5 mM EDTA, 1% SDS, 400 mM NaCl) supplemented with 0.5 mg ml^{-1} proteinase K, and the solution was incubated at 50 °C with occasional shaking for 1 h. After incubation, the solution was mixed with 400 µl phenol chloroform, vortexed for 15 s, and centrifuged at 14,000*g* for 30 s. The top aqueous layer of the mixed solution was removed and mixed with 40 µl of 3 M sodium acetate pH 5.4, 0.5 µl GlycoBlue (Thermo Scientific) and 750 µl isopropanol. The mixed solution was incubated at −20 °C for 20 min, then centrifuged at 14,000*g* for 30 s. The supernatant was removed and the pellet was washed with 400 µl ethanol and further centrifuged at 14,000*g* for 30 s. The supernatant was discarded and the tube was air-dried at room temperature for 20 min. Finally, 50 µl distilled water was added into the tube to dissolve the pellet, and the solution was used as template for polymerase chain reaction (PCR) using in-house-designed primers to amplify the DNA fragments that contained hIAPP genomic DNA (gDNA). The PCR products were sequenced by Laragen (USA).

The sequencing experiments were performed independently three times using three independent PCR products, and all results show that the genotype of hIAPP from donor 6 is the wild type. One of the representative sequencing results is given in the following, where the sequence of a part of the genome DNA that contains hIAPP gDNA is shown:

…AAAAAAAAATCTCAGCCATCTAGGTGTTTGCAAACCAAAACAC-TGAGTTACTTATGTGAAAATTGTTTCTTTGGTTTTCATCAATACAAGATA-TTTGATGTCACATGGCTGGATCCAGCTAAAATTCTAAGGCTCTAACTTTT-CACATTTGTTCCATGTTACCAGTCATCAGGTGGAAAAGCGGAAATGCA-ACACTGCCACATGTGCAACGCAGCGCCTGGCAAATTTTTTAGTTCATTCC AGCAACAACTTTGGTGCCATTCTCTCATCTACCAACGTGGGATCCAATAC ATATGGCAAGAGGAATGCAGTAGAGGTTTTAAAGAGAGAGCCACTGAATT ACTTGCCCCTTTAGAGGACAAT…

Fibrils extraction from islet cells and immunoprecipitation. The fibril extraction was performed according to a previous protocol[43]. Frozen islet cells were resuspended with 700 µl of saline buffer (0.15 M NaCl), homogenized and centrifuged at 19,000*g* at 4 °C for 20 min. The supernatant was removed (referred to as the S1 fraction) and the pellet was resuspended with 400 µl saline buffer, homogenized and centrifuged as in the previous step. The supernatant was also removed (referred to as the S2 fraction) and this 400-µl saline wash step was repeated another five times (generating S3–S7 fractions). The pellet was further washed three times with 400 µl H_2O with the same operation (generating S8–S10 fractions). The final pellet was lyophilized and then redissolved with 100 µl TBS buffer (20 mM Tris pH 7.6, 150 mM NaCl) and is referred to as the pellet (P). We found that the hIAPP fibrils are enriched mainly in the S1 fraction but not in the pellet, as described previously[43] by dot-blot assays and negative-stain EM (Extended Data Fig. 1b,c). We think this discrepancy is a consequence of the different tissues used for fibril extraction. In the previous study, frozen pancreatic tissues were used[43], whereas we used purified islet cells instead. In our case, the fibrils may be isolated much more easily, remaining in the supernatant of the first homogenization step. To assess the purity of the S1 fraction, we performed sodium dodecyl sulfate polyacrylamide gel electrophoresis (SDS–PAGE) and ran a western blot, probing with antibodies that target hIAPP, amyloid-β, tau or α-synuclein (Extended Data Fig. 9a). The results suggest that only hIAPP fibrils were present in the S1 fraction, enabling further purification of the S1 fraction via immunoprecipitation with fibril-binding OC antibody.

Before immunoprecipitation, we treated the S1 fraction with collagenase by mixing 60 µl of the S1 fraction with 60 µl TBS buffer supplemented with 4 µM $CaCl_2$ and 50 U ml^{-1} collagenase (Sigma). We then incubated the mixed solution for 1 h at 37 °C. To pull down amyloid fibrils, we first prepared the antibody-coupled magnetic beads by incubating 2 µg of anti-amyloid fibrils OC antibody (Millipore, lot no. 2345063) with 50 µl of protein A magnetic beads (Invitrogen) and diluted them in TBST buffer (20 mM Tris pH 7.6, 150 mM NaCl, 0.1% Tween 20) to a final volume of 700 µl, then the mixed solution was incubated on a tube rotator at room temperature for 1 h. After incubation, we collected the magnetic beads, discarded the supernatant, mixed the beads with 120 µl of collagenase-treated S1 fraction, and diluted the solution to final volume of 200 µl with TBS buffer. The final solution was incubated on a tube rotator at room temperature for 2 h, and the beads were then collected (the supernatant was removed and is referred to as the flowthrough fraction). The collected beads were first eluted with 150 µl TBST buffer (elute-1 fraction), then eluted twice with 50 µl of 100 mM glycine pH 2.0, and neutralized with 1 M Tris-HCl pH 9.0 (elute-2 and elute-3 fractions). The eluted beads were resuspended with 50 µl TBS and are referred to as the beads fraction. We found that the hIAPP fibrils were enriched in the elute-1 fraction, as judged by three criteria: (1) the observation of amyloid fibrils in electron micrographs, (2) the competence of the elute-1 fraction in seeding the aggregation of fresh hIAPP monomers and (3) positive anti-hIAPP and OC signals in dot blots compared to the absence of primary antibody (Fig. 1b,c, Extended Data Fig. 1d–f and Supplementary Text 6).

We note that the existence of hIAPP fibrils in the elute-2 fraction cannot be fully ruled out by dot blot, as the elute-2 fraction already contained a certain amount of OC antibody (as shown in the 'no primary' line in Extended Data Fig. 1d as a negative control) and the signal might be saturated, whereas in EM and seeding assays the elute fractions did not suggest the presence of hIAPP fibrils compared to the elute-1 fraction (Extended Data Fig. 1d–f). We believe the reason that hIAPP fibrils were not enriched in the elute-2 or elute-3 fractions is that the binding between hIAPP fibrils and OC antibody is not very strong, so that after the hIAPP fibrils were pulled down from the solution they could be easily separated from the antibody when a slight buffer change occurred during the elute-1 step (from half diluted TBS to TBST, see above for details), before a larger buffer change occurred at the elute-2 or elute-3 step.

Dot blot and western blot. In our dot-blot assay, 2 µl of each sample solution was pipetted onto multiple nitrocellulose membranes (Invitrogen) in parallel and allowed to dry for 15 min. The membranes were probed by amylin polyclonal antibody (also referred to as anti-hIAPP antibody in this study, Invitrogen, lot no. UH2833361, 1:1,000 dilution) or anti-amyloid fibril OC antibody (Millipore, lot no. 2345063, 1:5,000 dilution) respectively, and further probed by anti-rabbit immunoglobulin-G (Sigma, lot no. 023M4757, 1:5,000 dilution) as the secondary antibody, and visualized with an ECL Plus western blotting substrate kit (Thermo Scientific). For an explanation for the high intensity in the 'no background' dot blot of elute-2 (Extended Data Fig. 1d), see Supplementary Text 6.

In Extended Data Fig. 9a, we used western blot to analyze the molecular weight of the S1 fraction. The loading dye contained 2 M urea. Proteins were transferred to nitrocellulose membranes (Invitrogen) and detected by immunoblot analysis with amylin polyclonal antibody (Invitrogen, lot no. UH2833361, 1:1,000 dilution), anti-tau antibody (Agilent Dako, lot no. 20024929, 1:5,000 dilution), anti-amyloid-β antibody 6E10 (Biolegend, lot no. B261546, 1:5,000 dilution) and anti-α-synuclein antibody (MJFR-14-6-4-2, Abcam, lot no. GR3222269-10, 1:5,000 dilution). As a secondary antibody we used goat anti-rabbit horseradish peroxidase (HRP; Invitrogen, lot no. 2116291, 1:5,000 dilution) or goat anti-mouse HRP (Abcam, lot no. GR3271082-2, 1:5,000 dilution). All membranes were developed using Pierce ECL Plus substrate (Thermo Scientific). We used positive controls to validate the antibodies for amyloid-β1–42 (expected size ~4 kDa, for anti-amyloid-β antibody), tau-K18 (residues 244–372, expected size ~15 kDa, for anti-tau antibody) and α-synuclein 1–140 (expected size ~14 kDa, for anti-α-synuclein antibody).

Negative-stain transmission electron microscopy. Negative-stain transmission EM samples were prepared by applying 5 µl of solution to 400-mesh carbon-coated formvar support films mounted on copper grids (Ted Pella). The grids were glow-discharged for 30 s before applying the samples. The samples were incubated on the grid for 2 min and then blotted off with filter paper. The grids were stained with 3 µl of 2% uranyl acetate for 1 min and washed with an additional 3 µl of 2% uranyl acetate and allowed to dry for 1 min. The grids were imaged using a T12 (FEI) electron microscope.

Synthetic hIAPP preparation. Synthetic full-length hIAPP peptide was ordered from InnoPep with an amidated C terminus and a disulfide bond between Cys2 and Cys7, and the purity was >95%. The peptide was dissolved in 100% 1,1,1,3,3,3-hexafluoro-2-propanol (HFIP) at a concentration of 1 mM, sonicated at 4 °C for 1 min, and incubated at room temperature for 5 h. After incubation, HFIP was evaporated by a CentriVap concentrator (Labconco) and the peptide was stored at −20 °C. Before use, HFIP-treated peptide was dissolved in 100% DMSO at a concentration of 1 mM or 5 mM, and further diluted 100-fold in phosphate-buffered saline (PBS) and filtered with 0.1 µm Ultrafree-MC-VV centrifugal filters (Millipore) to form 10 µM and 50 µM hIAPP solutions.

Thioflavin T (ThT) seeding assays. Synthetic hIAPP was diluted to 10 μM or 50 μM in PBS supplemented with 30 μM ThT, filtered with 0.1-μm Ultrafree-MC-VV centrifugal filters (Millipore) and mixed with 1% or 5% (vol/vol) of seeds, respectively. The seeds were sonicated at 4 °C for 3 min before use. Mixed solution was pipetted into a Polybase Black 384-well plate with an optical bottom (Thermo Scientific) and incubated at 37 °C without shaking. ThT fluorescence was monitored by a FLUOstar Omega plate reader (BMG LABTECH) with excitation and emission wavelengths of 440 nm and 480 nm, respectively. The fluorescence curves were averaged from three independent measured replicates, and error bars show s.d. of replicate readings. To normalize the different ranges of fluorescence readings observed from different experiments (probably due to the different fluorescence gain settings of the plate reader), we normalized the readings to make the minimum mean value in each panel 0% and the maximum mean value in each panel 100%. To test the seeding ability of different fractions from the immunoprecipitation assay, 10 μM hIAPP solution was mixed with 1% (vol/vol) of the fractions (elute-1, elute-2 and elute-3) as fibril growing seeds (results are shown in Extended Data Fig. 1f). To monitor the seeding effect at the same concentration as growing fibrils for cryo-EM structure determination, 50 μM hIAPP solution was mixed with or without 5% (vol/vol) of the elute-1 fraction from immunoprecipitation as the patient extract (shown in Fig. 1c). ThT curves were generated using GraphPad Prism.

Fibril growth and seeding. To obtain the high fibril yields necessary for cryo-EM studies, we raised the concentration of hIAPP monomers from the 10 μM used in the seeding assays shown in Extended Data Fig. 1f to 50 μM. We were concerned that the elevated concentration of hIAPP would enhance the growth of unseeded amyloid fibrils and divert monomer from being templated by the seed. However, we found that seeding at this elevated hIAPP concentration still had a strong effect. It notably increased the aggregation rate and ThT signal compared to the monomers incubated in the absence of seeds (Fig. 1c). On imaging samples prepared by 20 h of incubation, we found the monomers incubated with seeds show mature and elongated fibrils, whereas the monomers incubated alone show immature fibrils (Fig. 1d). This observation further suggested the efficacy of seeding.

Freshly diluted and filtered 50 μM hIAPP solution in PBS was mixed with 5% (vol/vol) patient extract as seeds. The seeds were sonicated at 4 °C for 3 min before use. The solution was then incubated at 37 °C without shaking for 20 h. After incubation, the solution was centrifuged at 4,000*g* for 1 min, and 95% of the original volume of supernatant was carefully removed from the centrifuge tube to concentrate the fibril solution 20 times. The remaining fibrils were resuspended by mixing with a pipette and then used for cryo-EM data collection. We tested the cytotoxicity of the seeded fibrils used in cryo-EM by 3-[4,5-dimethylthiazol-2-yl]-2,5 diphenyl tetrazolium bromide (MTT) assays (Extended Data Fig. 9b).

Cryo-electron microscopy data collection and processing. To prepare the grids for cryo-EM data collection, we applied 2.6 μl of fibril solution onto a Quantifoil 1.2/1.3 electron microscope grid, which had been glow-discharged for 2 min before use. The grid was plunge-frozen in liquid ethane with a Vitrobot Mark IV instrument (FEI). Two datasets were collected on the same 300-kV Titan Krios (FEI) microscope with a Gatan K3 camera located at the HHMI Janelia Research Campus, and were collected from grids that were made in parallel from the same batch of fibril samples. The microscope was operated with 300 kV acceleration voltage and a slit width of 20 eV. Videos were collected using super-resolution mode with a nominal physical pixel size of 1.065 Å per pixel (0.5325 Å per pixel in super-resolution video frames) with a dose per frame of ~1.5 $e^-/Å^2$. Fifty-seven frames were taken for each video for the first dataset (total dose per image ~85.5 $e^-/Å^2$) and 30 frames were taken for each video for the second dataset (total dose per image of ~45 $e^-/Å^2$). Automated data collection was driven by SerialEM[44]. Anisotropic magnification distortion estimation, CTF estimation and beam-induced motion correction were performed with mag-distortion-estimate[45], CTFFIND 4.1.8[46] and Unblur[47], respectively. The physical pixel size was corrected to 1.055 Å per pixel after anisotropic magnification correction with Unblur[47].

Particle picking was performed manually using EMAN2 e2helixboxer.py[48] for the first dataset, and performed automatically using CrYOLO[49] for the second dataset. Particle extraction, 2D classification, helical reconstruction and 3D refinement were performed in RELION[50,51]. Particles were extracted using an inter-box distance of 14.1 Å and a box size of 768 pixels that downscaled to a box size of 384 pixels (bin factor equal to 2). We performed 2D classification with tau_fudge factor set to 2, and from 2D classes we were able to identify four morphologies with twisting features and another four morphologies without twisting features (TW1–4 and NT1–4, respectively; Fig. 2 and Extended Data Fig. 2). The disruption of each morphology is shown in Fig. 2 (inset). We were only able to pursue the morphologies with twisting features due to the limitation of helical reconstruction. We selected the particles that belonged to 2D classes of TW1–4 and re-extracted them (individually for each morphology) into a box size of 256 pixels (for TW1, TW3 and TW4, which have relatively short pitch) or 384 pixels (for TW2, which has relatively long pitch). No downscaling was used for re-extraction, and the inter-box distance was kept to 14.1 Å. The helical parameters of each twister morphology were estimated from the measured crossover distance and used for further 3D classification. We performed 3D classification with $K=3$ (or $K=5$ for TW2) and a Gaussian cylinder initial model as described previously[12]. Particles belonging to the best 3D class were selected, and several more rounds of 3D classification ($K=3$) were performed for each TW morphology to make sure the best particles were selected. The tau_fudge factor was set to 4 at the beginning of each 3D job, and was increased to 64 to push the resolution of the reconstructions. We then used the particles selected from the 3D classification to perform high-resolution gold-standard refinement[51], and the resolution of each reconstruction was estimated using the 0.143 Fourier shell correlation (FSC) resolution cutoff. Before performing gold-standard refinement of TW2, we re-extracted the selected particles from a pixel box size of 384 to a pixel box size of 256 to obtain a higher-quality final map.

Previous structural studies of unseeded synthetic wild-type hIAPP fibrils show structures that are similar to TW3 (PDB 6Y1A[15] and 6ZRF[16]; Extended Data Fig. 4b), but their two structures were reconstructed with different handedness (right-handed twist for 6Y1A[15] and left-handed twist for 6ZRF[16]). Because, in this study, we were not able to achieve resolutions high enough to identify the handedness of each morphology, here we performed reconstructions by assuming all the TW morphologies are left-handed, as the left-handed twist is most common for amyloid fibrils. We cannot rule out the possibility that one or serval of the TW morphologies solved here are right-handed. We believe that handedness should not influence the model we build for each morphology, as in the current resolution the same fold can be generated with either handedness, which is supported by the observation that 6Y1A and 6ZRF adopt a similar structure but have different handedness. We thus believe that determining the handedness should be beyond the scope of this study, as we mostly focus on the structures within each layer of the fibrils.

Atomic model building. The refined maps were sharpened with phenix.auto_sharpen[52] at the resolution cutoff indicated by half-map FSC. The atomic model of each TW morphology was manually built into the sharpened map using COOT[53]. For TW1, the map clearly suggests that a single layer contains two asymmetric chains. To build each chain, we first located the C-terminal tyrosine residue (Tyr37) at the end of the density tube that does not have extra fuzzy density. The remaining residues were built de novo according to their position in sequence relative to Tyr37. The resulting model fits the map unambiguously for all side chains (except a bump in TW1, Supplementary Text 7). Atomic model building of TW2 to TW4 is also described in Supplementary Text 7 (Extended Data Fig. 10).

The initial models were extended to five layers (10 chains) based on the helical symmetry of each TW morphology, and the five-layer models were refined by phenix.real_space_refine[54] for several rounds. As the last step, the rotamer of each serine, glutamine and asparagine residue was manually inspected to favor hydrogen bonds, and the final model was validated using MolProbity[55].

Structural alignment of all reported hIAPP fibril structures. With the four structures reported in this study there are currently nine near-atomic resolution structures of hIAPP fibrils (Table 2). To reduce the amount of structures used for comparison, we used TW3 to represent 6Y1A[15] and 6ZRF[16], because these three structures are very similar to each other (Extended Data Fig. 4b). Furthermore, two morphologies from hIAPP S20G fibrils have an almost identical conformation of chain A and B (6ZRR and 6ZRQ[16]; 6ZRR has an additional chain C in each layer), so we used 6ZRR to represent 6ZRQ. Here, we performed structural alignment of these structures at the single-chain level. That is, for those structures that contain two identical monomers in each layer (such as TW3), only chain A was used for structural alignment; for structures that contain two monomers with different structures (such as TW1), both chains A and B were used for structural alignment; for 6ZRR, which contains two identical monomers (chains A and B) and one additional monomer with different fold (chain C), chain A and C were used for structure alignment. The alignment was done via PyMOL[56]. Initially, all residues in each chain were used for structural alignment, and after all chains had been categorized into CF1 and CF2, all chains with a CF1 fold were re-aligned with the residue range restricted to 15–28 and those with a CF2 fold were re-aligned with the residue range restricted to 20–33.

We note that our previously reported SUMO-tagged recombinant hIAPP fibril structure contained CF2 when the 'swapped' version was used for structural alignment. The swapped version of 6VW2 was proposed in our previous structure study of hIAPP fibrils[12], and is formed by swapping the residues from two chains in a single layer at Gly24 that are very close to each other (Extended Data Fig. 6; red dashed line in Fig. 3b); this domain swap is predicted to be chemically and energetically plausible, although not supported by the density map of 6VW2[12].

Note that we only use cryo-EM structures of hIAPP for structural comparison and analysis here, but there are models of hIAPP fibrils reported previously that were generated by different methods[13,14]. These alternate models, especially the one from the NMR study, may represent the structure of the ribbon morphology of hIAPP fibrils, which cannot be readily determined by cryo-EM. In our seeded fibrils, we also observed four morphologies of the ribbon form of hIAPP fibrils (NT1–4, Extended Data Fig. 2a,b), which together comprised 35% of the total population and were not amenable for cryo-EM structure determination. We cannot rule out the possibility that the structures of NT1–4 may be similar to the NMR model.

Structural alignment of hIAPP and amyloid-β fibril structures. The PDB IDs of the amyloid-β structures used for structural alignment are 6OIZ[57], 2M4J[58], 2MVX[59], 5KK3[60], 5OQV[61], 2NAO[62], 2MXU[63], 2BEG[64], 2LMN[65], 2MPZ[66] and 6SHS[67]. Structural alignment was done via PyMOL[56]. We aligned each amyloid-β structure with TW1 chain A, chain B and TW2 using residues 24–34 in each amyloid-β structure and residues 19–29 in hIAPP fibril structures. The r.m.s.d. values for each alignment are summarized in Supplementary Table 3.

MTT assays. Rin5F cells were purchased from ATCC (cat. no. CRL-2058), then 90 µl of cells were plated at 60,000 cells per ml, in 96-well plates (cat. no. 3603, Costar, Fisher Scientific) in DMEM medium (Life Technologies, cat. no. 11965092) supplemented with 10% (vol/vol) FBS (Life Technologies, cat. no. A3160401), 1% penicillin/streptomycin (Life Technologies, cat. no. 15140122) and 1% Glutamax (Life Technologies, cat. no. 35050061) at 37 °C, 5% CO_2, in a humidified incubator. To perform MTT assays, patient-fibril-seeded hIAPP fibrils at a concentration of 50 µM were pelleted by centrifugation at 21,000*g* for 1 h and supernatant was removed. The pellet was suspended in sterile PBS buffer and sonicated for 5 min, then 10 µl of sample solution was added to cells at various concentrations (0, 1, 10 and 50 µM). Experiments were performed in triplicate. After a 24 h incubation of samples with cells, 20 µl of Thiazolyl Blue tetrazolium bromide MTT dye (Sigma) was added to each well and incubated for 3.5 h at 37 °C under sterile conditions. The MTT dye stock was prepared by dissolving 5 mg ml^{-1} in sterile PBS buffer. The MTT assay was stopped by carefully aspirating off the culture medium and adding 100 µl of 100% DMSO to each well. Absorbance was measured at 570 nm and the background reading was recorded at 700 nm and subsequently subtracted from the value at 570 nm.

Statistics and reproducibility. The western blot, ThT and cytotoxicity experiments were replicated at least three times with similar results. We did not replicate the Congo red staining. One negative-stain EM grid was prepared and imaged for each sample, whereas multiple (more than three) micrographs with similar results were observed for each grid.

Reporting Summary. Further information on research design is available in the Nature Research Reporting Summary linked to this article.

Data availability

Structural data have been deposited into the Worldwide Protein Data Bank (wwPDB) and the Electron Microscopy Data Bank (EMDB) with the following accession codes: PDB 7M61, EMD-23686 (TW1); PDB 7M62, EMD-23687 (TW2); PDB 7M64, EMD-23688 (TW3); PDB 7M65, EMD-23689 (TW4). PDB accession codes for previously reported coordinates used for structural analysis in this study are: 6Y1A, 6ZRR, 6ZRQ, 6ZRF, 6VW2 for hIAPP fibrils and 6OIZ, 2M4J, 2MVX, 5KK3, 5OQV, 2NAO, 2MXU, 2BEG, 2LMN, 2MPZ, 6SHS for amyloid-β fibrils. All data are available in the paper or the Supplementary Information.

Code availability

Energetic calculations were performed using custom written software. The code is available at the MBI website (https://people.mbi.ucla.edu/sawaya/amyloidatlas/accessiblesurfacearea_v07.2d.f).

References

43. Johnson, K. H. et al. Feline insular amyloid: immunohistochemical and immunochemical evidence that the amyloid is insulin-related. *Vet. Pathol.* **22**, 463–468 (1985).
44. Mastronarde, D. N. Automated electron microscope tomography using robust prediction of specimen movements. *J. Struct. Biol.* **152**, 36–51 (2005).
45. Grant, T. & Grigorieff, N. Automatic estimation and correction of anisotropic magnification distortion in electron microscopes. *J. Struct. Biol.* **192**, 204–208 (2015).
46. Rohou, A. & Grigorieff, N. CTFFIND4: fast and accurate defocus estimation from electron micrographs. *J. Struct. Biol.* **192**, 216–221 (2015).
47. Grant, T. & Grigorieff, N. Measuring the optimal exposure for single particle cryo-EM using a 2.6-Å reconstruction of rotavirus VP6. *eLife* **4**, e06980 (2015).
48. Tang, G. et al. EMAN2: an extensible image processing suite for electron microscopy. *J. Struct. Biol.* **157**, 38–46 (2007).
49. Wagner, T. et al. Two particle-picking procedures for filamentous proteins: SPHIRE-crYOLO filament mode and SPHIRE-STRIPER. *Acta Crystallogr. D Struct. Biol.* **76**, 613–620 (2020).
50. He, S. & Scheres, S. H. W. Helical reconstruction in RELION. *J. Struct. Biol.* **198**, 163–176 (2017).
51. Scheres, S. H. W. RELION: implementation of a Bayesian approach to cryo-EM structure determination. *J. Struct. Biol.* **180**, 519–530 (2012).
52. Terwilliger, T. C., Sobolev, O. V., Afonine, P. V. & Adams, P. D. Automated map sharpening by maximization of detail and connectivity. *Acta Crystallogr. D Struct. Biol.* **74**, 545–559 (2018).
53. Emsley, P., Lohkamp, B., Scott, W. G. & Cowtan, K. Features and development of Coot. *Acta Crystallogr. D. Biol. Crystallogr.* **66**, 486–501 (2010).
54. Afonine, P. V. et al. Real-space refinement in PHENIX for cryo-EM and crystallography. *Acta Crystallogr. D Struct. Biol.* **74**, 531–544 (2018).
55. Chen, V. B. et al. MolProbity: all-atom structure validation for macromolecular crystallography. *Acta Crystallogr. D Biol. Crystallogr.* **66**, 12–21 (2010).
56. The PyMOL Molecular Graphics System, Version 1.8 (Schrödinger, 2015).
57. Warmack, R. A. et al. Structure of amyloid-β (20-34) with Alzheimer's-associated isomerization at Asp23 reveals a distinct protofilament interface. *Nat. Commun.* **10**, 3357 (2019).
58. Lu, J.-X. et al. Molecular structure of β-amyloid fibrils in Alzheimer's disease brain tissue. *Cell* **154**, 1257–1268 (2013).
59. Schutz, A. K. et al. Atomic-resolution three-dimensional structure of amyloid β fibrils bearing the Osaka mutation. *Angew. Chem. Int. Ed.* **54**, 331–335 (2015).
60. Colvin, M. T. et al. Atomic resolution structure of monomorphic Aβ42 amyloid fibrils. *J. Am. Chem. Soc.* **138**, 9663–9674 (2016).
61. Gremer, L. et al. Fibril structure of amyloid-β(1–42) by cryo-electron microscopy. *Science* **358**, 116–119 (2017).
62. Walti, M. A. et al. Atomic-resolution structure of a disease-relevant Aβ(1–42) amyloid fibril. *Proc. Natl Acad. Sci. USA* **113**, E4976–E4984 (2016).
63. Xiao, Y. et al. Aβ(1–42) fibril structure illuminates self-recognition and replication of amyloid in Alzheimer's disease. *Nat. Struct. Mol. Biol.* **22**, 499–505 (2015).
64. Luhrs, T. et al. 3D structure of Alzheimer's amyloid-β(1–42) fibrils. *Proc. Natl Acad. Sci. USA* **102**, 17342–17347 (2005).
65. Paravastu, A. K., Leapman, R. D., Yau, W.-M. & Tycko, R. Molecular structural basis for polymorphism in Alzheimer's β-amyloid fibrils. *Proc. Natl Acad. Sci. USA* **105**, 18349–18354 (2008).
66. Sgourakis, N. G., Yau, W.-M. & Qiang, W. Modeling an in-register, parallel 'iowa' aβ fibril structure using solid-state NMR data from labeled samples with rosetta. *Structure* **23**, 216–227 (2015).
67. Kollmer, M. et al. Cryo-EM structure and polymorphism of Aβ amyloid fibrils purified from Alzheimer's brain tissue. *Nat. Commun.* **10**, 4760 (2019).

Acknowledgements

We thank the Southern California Islet Cell Resources Center for providing human islets for this study. We thank X. Zhao at the HHMI Janelia Cryo-EM Facility for help with microscope operation and data collection. We acknowledge support from NIH AG 054022, NIH AG061847 and DOE DE-FC02-02ER63421. D.R.B. was supported by the National Science Foundation Graduate Research Fellowship Program.

Author contributions

Q.C. designed experiments and performed data analysis. F.K. prepared islet cells from donors. Q.C. and L.S. performed Congo red staining of islet cells. Q.C., L.S. and B.A.N. performed fibril extraction from islet cells. Q.C. and R.A. performed immunoprecipitation in fibril extraction. R.A. and J.L. performed western blot and MTT assays. K.A.M. helped with western blots. Q.C. prepared hIAPP fibrils and cryo-EM grids. Q.C. and D.R.B. collected cryo-EM data. Q.C. performed cryo-EM data processing and model building, J.L. assisted with particle picking. Q.C. and M.R.S. performed solvation energy calculations. All authors analyzed the results and wrote the manuscript. D.S.E. supervised and guided the project.

Competing interests

D.S.E. is an advisor and equity shareholder in ADRx, Inc. The remaining authors declare no competing interests.

Additional information

Extended data is available for this paper at https://doi.org/10.1038/s41594-021-00646-x.

Supplementary information The online version contains supplementary material available at https://doi.org/10.1038/s41594-021-00646-x.

Correspondence and requests for materials should be addressed to David S. Eisenberg.

Peer review information *Nature Structural & Molecular Biology* thanks Sjors Scheres and the other, anonymous, reviewer(s) for their contribution to the peer review of this work. Peer reviewer reports are available.

Reprints and permissions information is available at www.nature.com/reprints.

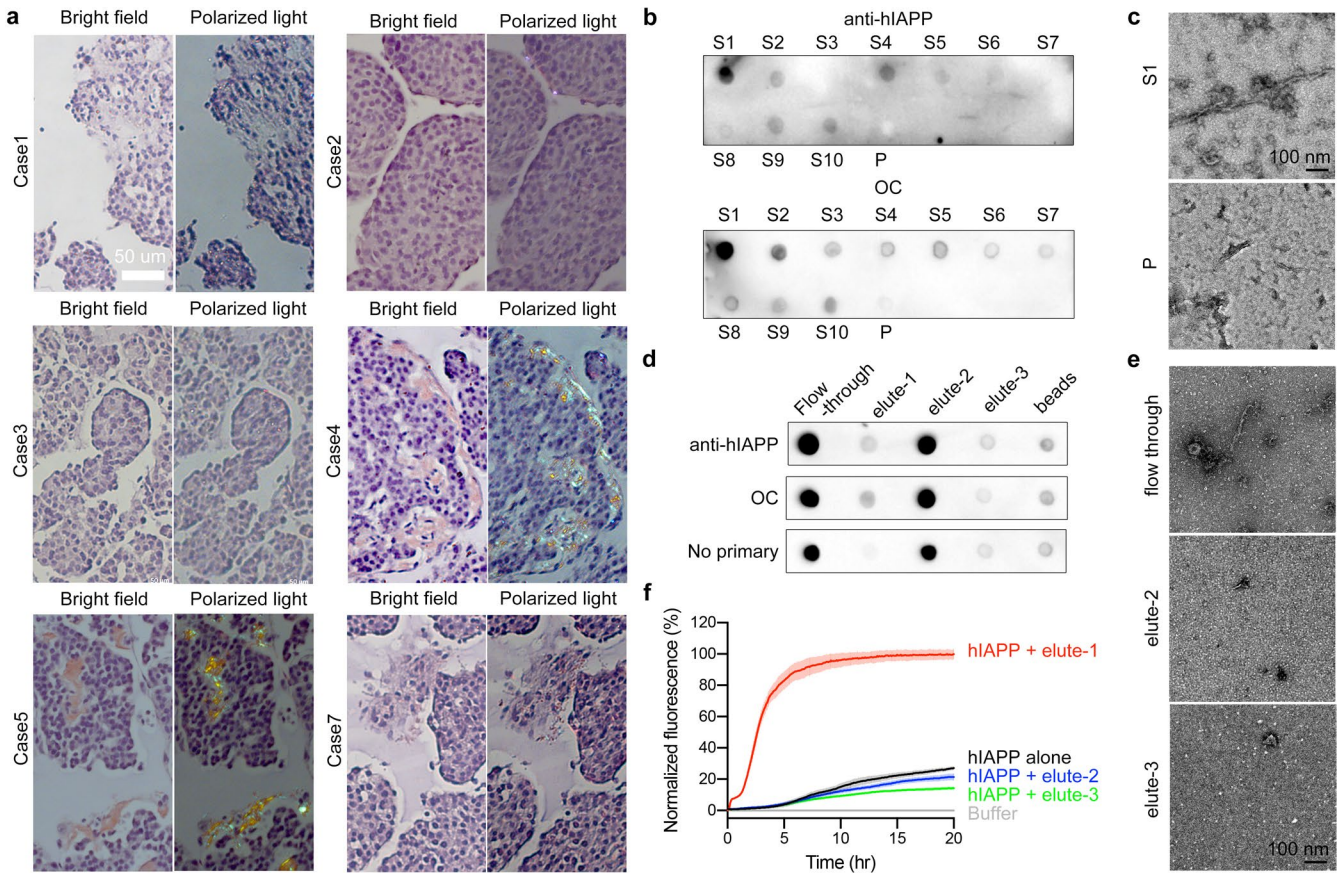

Extended Data Fig. 1 | Supplemental information on extraction of patient islet cells and seeding of fibril growth. a, Congo Red staining of slices of islet cells from various T2D donors (see Supplementary Table 1). **b**, Dot blot of fractions from extracted patient islet cells probed by anti-hIAPP (top) and anti-amyloid fibrils OC (bottom) antibodies. **c**, Negatively stained images of S1 and P fractions in (**b**). **d**, Dot blot of fractions from immunoprecipitation of the S1 fraction probed by anti-hIAPP (top), OC (middle) antibodies and no primary antibody (bottom) as a base line. **e**, Negatively stained images of flow through, elute−2 and elute−3 fractions in (**b**). The EM image of the elute−1 fraction is shown in Fig. 1b. **f**, ThT aggregation curves of fresh prepared synthetic hIAPP peptide incubated alone (black) or with elute-1 (red), elute-2 (blue) or elute-3 (green) fraction in (**d**) as fibril growth seeds. Data are shown as mean ± s.d., n=3 independent experiments. Note the elute-1 fraction from immunoprecipitation shows notable seeding ability as its curve shows shortened lag time and stronger ThT readings compared to hIAPP alone, whereas the elute-2 and elute-3 fractions show no ability in altering the hIAPP aggregation curve. Please see methods for the detailed definitions of fractions in panels **b**–**f**.

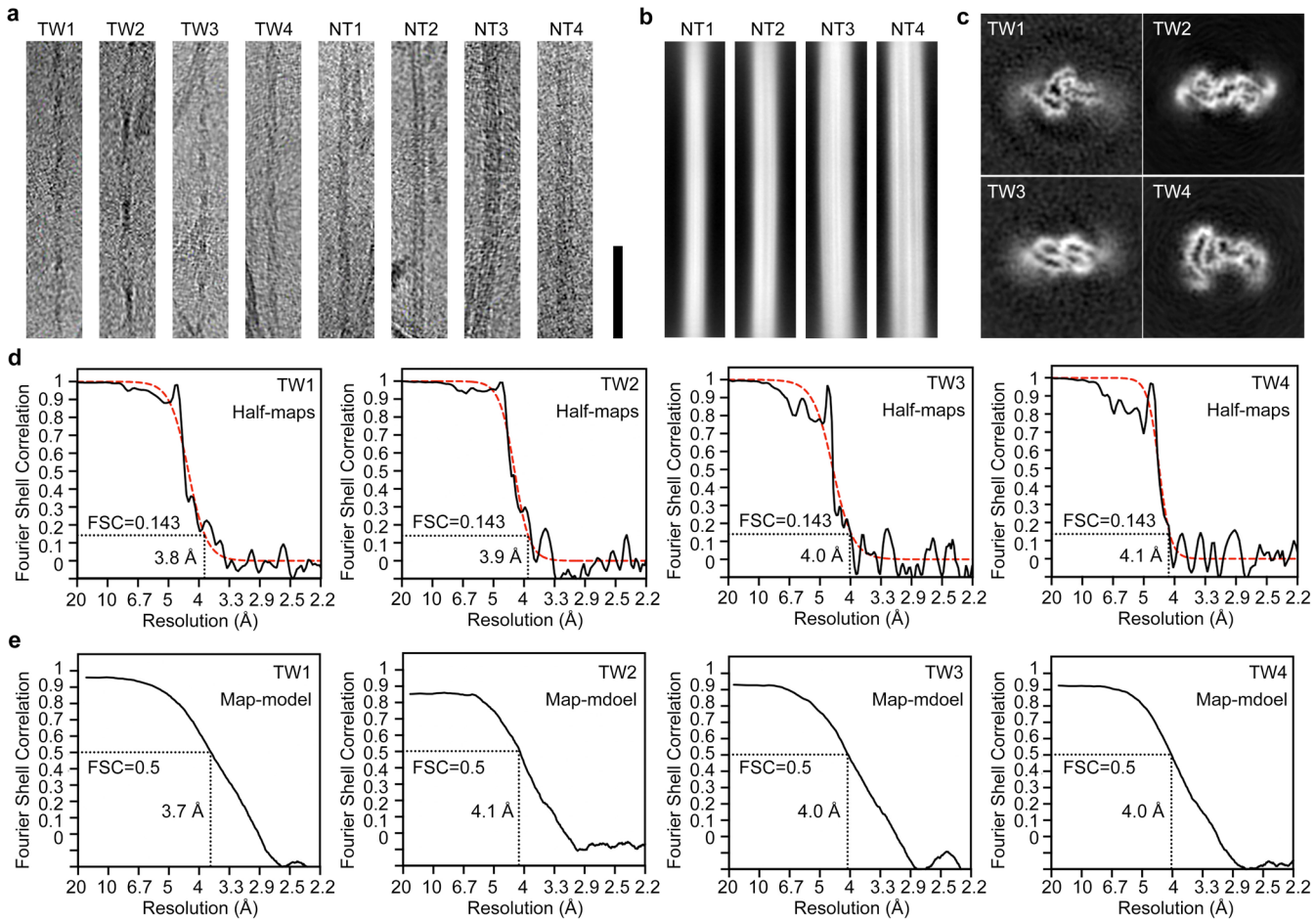

Extended Data Fig. 2 | Cryo-EM data processing. a, Representative micrographs of 8 identifiable morphologies during data processing (TW1-TW4 and NT1-NT4, scale bar 500 Å). **b**, Representative 2D classes of NT1-NT4. **c**, Central slices of final 3D reconstructions of TW1-TW4. **d**-**e**, FSC curves between two half-maps (**e**) and the cryo-EM reconstruction and refined atomic model (**f**). In half-maps FSC, FSC curves (black) are fitted (red) with the model function 1/(1+exp((x-A)/B)), with A=0.2328 and B=0.01517 for TW1, A=0.2347 and B=0.01234 for TW2, A=0.2255 and B=0.01427 for TW3, and A=0.2252 and B=0.009377 for TW4.

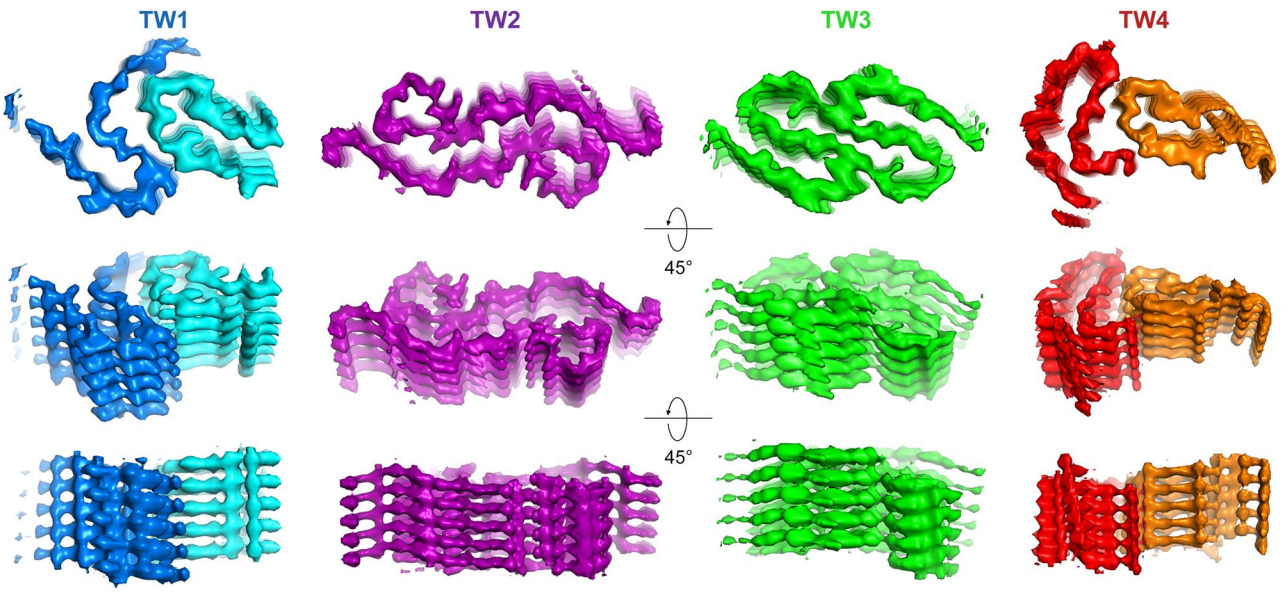

Extended Data Fig. 3 | Different views of the cryo-EM maps with five layers shown. For each morphology, the top view shows clear separation of β-strands, and the tilted views on the middle and bottom show clear separation of the layers of β-sheets along the fibril axis.

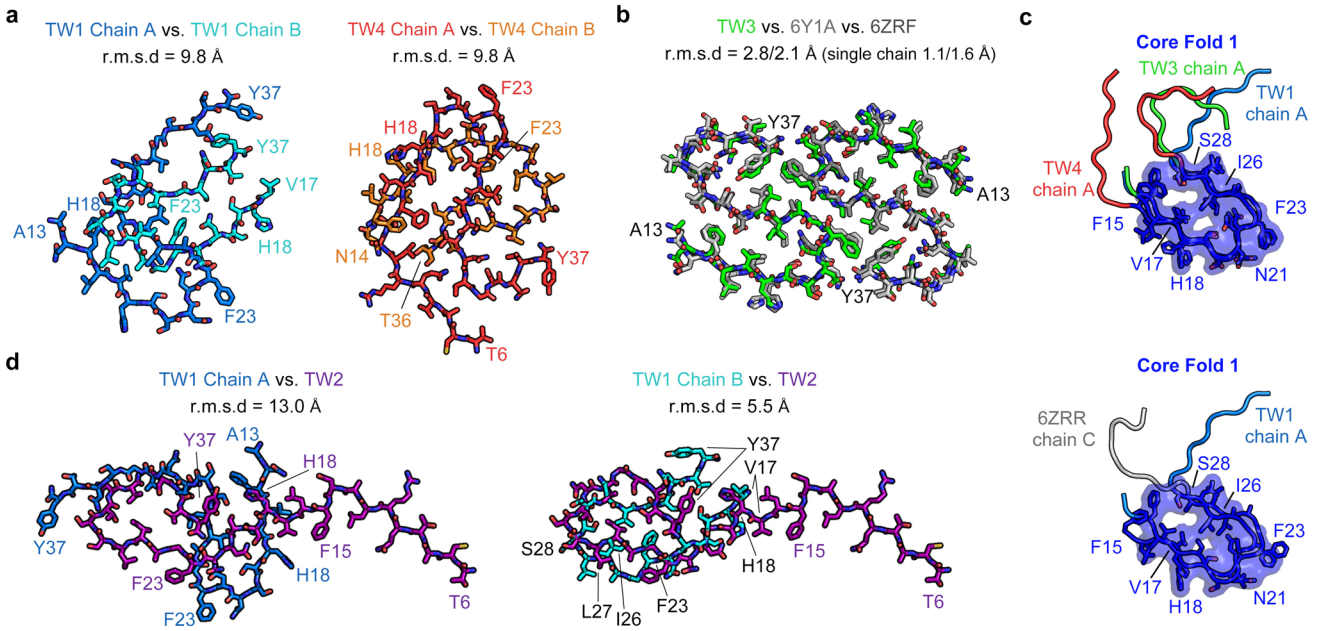

Extended Data Fig. 4 | Structural comparisons of hIAPP fibrils. a, Superposition of chain A and B of TW1 (left) and TW4 (right). **b**, Superposition of TW3, 6Y1A and 6ZRF, note that these three structures are very similar to each other. **c**, Superposition of chain A of TW1, TW3 and TW4 (top) and of TW1 chain A and 6ZRR chain C (bottom) at CF1 region. **d**, Superposition of TW1 chain A and TW2 (left), or TW1 chain B and TW2 (right). For superimposition details of panels **a**, **b** and **d** see Supplementary Table 2.

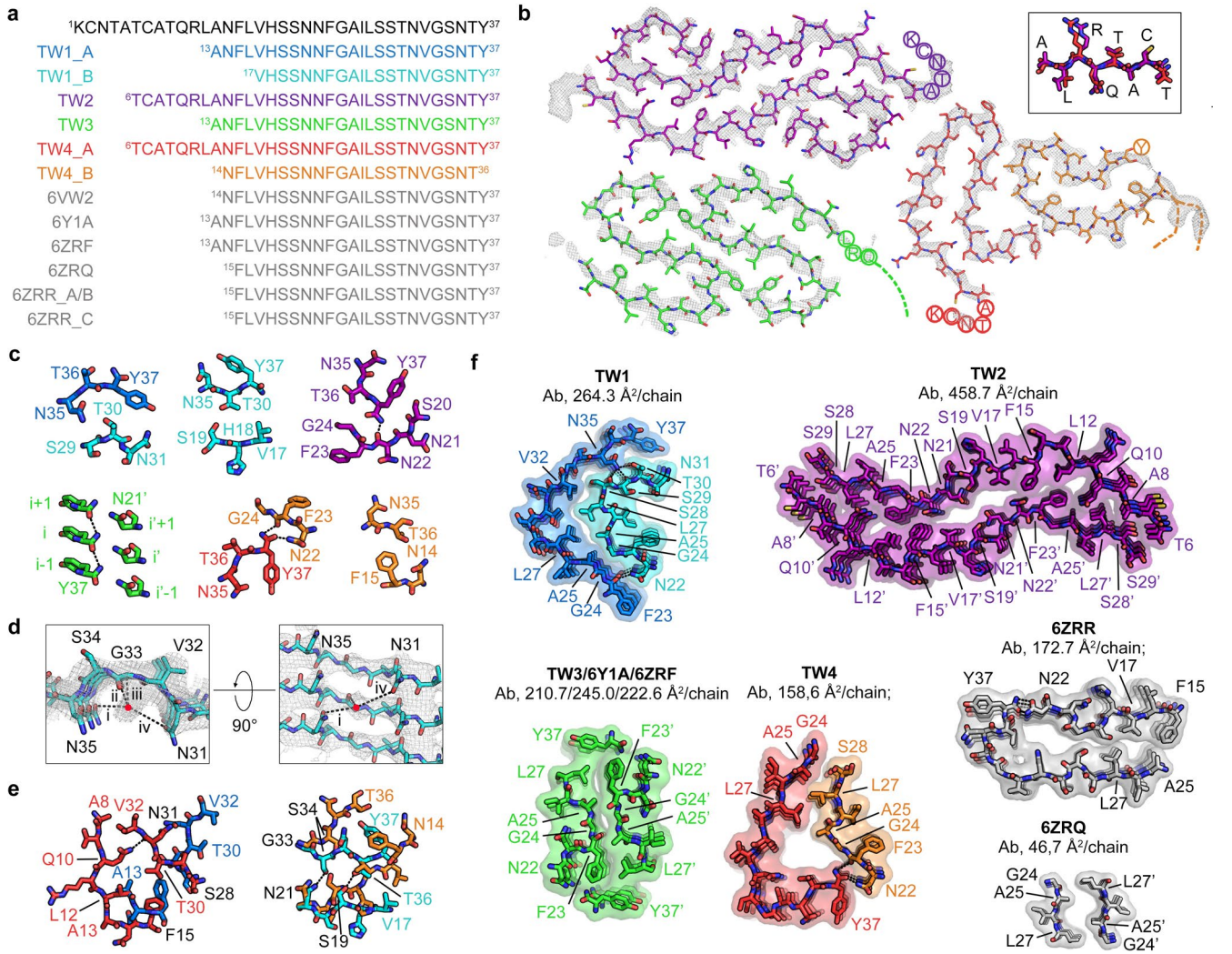

Extended Data Fig. 5 | Detailed analysis of hIAPP fibril structures. a, Above in black: the amino acid sequence of hIAPP; below: the residues visible in different hIAPP fibril structures. **b**, Plausible conformations of flexible N-termini of TW2 (purple), TW3 (green) and TW4 (red and orange) suggested by weak densities. The superposition of Thr6 to Ala13 region of TW2 and TW4 chain A is shown as an insert. **c**, The interactions around Tyr37 for TW1 (chain A, blue; chain B, cyan), TW2 (purple), TW3 (green), and TW4 (chain A, red; chain B, orange). **d**, The detailed view of an unexplained density around Gly33. The red dot represents the center of the unexplained density, and the length of each dash line is: i, 4.0 Å; ii, 2.9 Å; iii, 3.7 Å; iv, 5.2 Å. **e**, Different conformations of chain A of TW1 (marine) and TW4 (red, left) or chain B of TW1 (cyan) and TW4 (orange, right) outside the CF1 or CF2 region, respectively. TW1 and TW2 are superimposed at the CF1 (chain A) or CF2 (chain B) region. **f**, The interfaces between protofilaments A and B for TW1 (marine and cyan), TW2 (purple), TW3 (green), TW4 (red and orange), and 6ZRQ (gray), as well as between protofilaments B (top) and C (bottom) for 6ZRR (grey). Ab, area buried. In panels **c**, **e**, and **f**, hydrogen bonds with distances between 2.3 and 3.2 Å are shown as black dashed lines. For superimposition details for panel **b** see Supplementary Table 2.

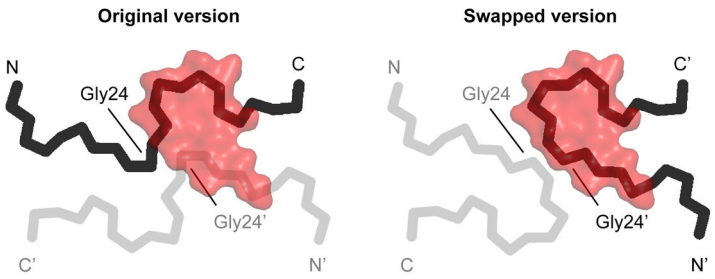

Extended Data Fig. 6 | Explanation of swapped version of 6VW2. Original version (left) and swapped version (right) of SUMO-tagged recombinant hIAPP fibril structure. Two symmetrically related chains are colored black and grey. CF2 was shown as surface and colored red.

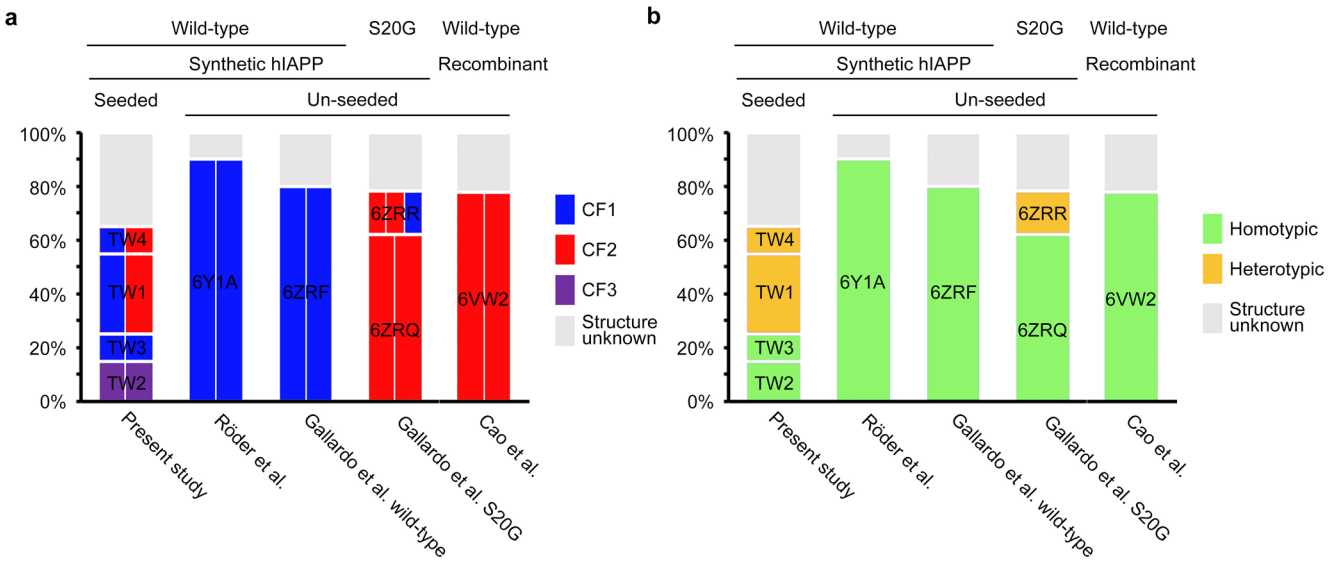

Extended Data Fig. 7 | Distribution of different polymorphs in reported hIAPP cryo-EM datasets. hIAPP polymorphs are colored by (**a**) core folds or (**b**) homotypic vs. heterotypic pairings. From panel **a**, we found CF2 is more abundant in S20G dataset compared to wildtype ones with the exception of 6VW2 dataset. In S20G dataset, 6ZRQ contributes to 76% of the solvable fibrils and is purely composed of protofilaments with CF2; 6ZRR contributes to the other 24% and contains two protofilaments with CF2 and one protofilament with CF1. In contrast, wild-type fibrils, 6ZRF and 6Y1A are the only solvable species in their datasets and they contain only CF1 in their protofilaments; in the wild-type fibrils in this study, we also observe more protofilaments with CF1 than that with CF2. TW1 and TW4 have equal amount of protofilaments with CF1 and CF2, but TW3 contains only protofilaments with CF1. From panel **b**, we note when formed in vitro without patient seeds, we observed homo-dimer forms of fibrils in most datasets (Cao et al., Röder et al., and the wile-type of Gallardo et al.) and only in one dataset did we find a small portion of heterotypic species (S20G of Gallardo et al., in which 6ZRR contributes to 24% of the solvable population compared to 76% of 6ZRQ that is homo-dimer form). Whereas in patient-extract-seeded fibrils we see higher populations of heterotypic species (TW1 and TW4 contribute to 40% out of 65% of solvable population).

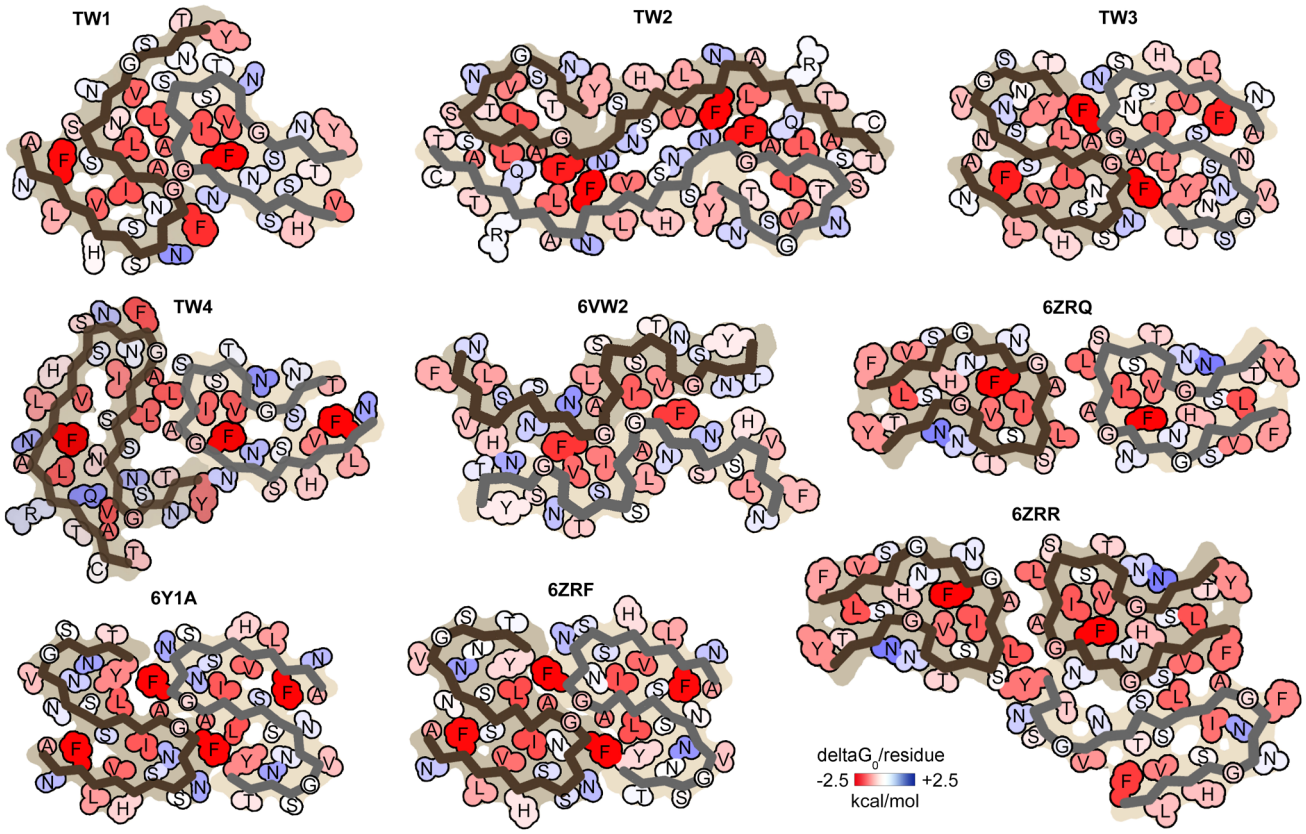

Extended Data Fig. 8 | Solvation energy maps of reported cryo-EM hIAPP fibril structures. Residues are colored from unfavorable (blue, 2.5 kcal/mol) to favorable stabilization energy (red, −2.5 kcal/mol).

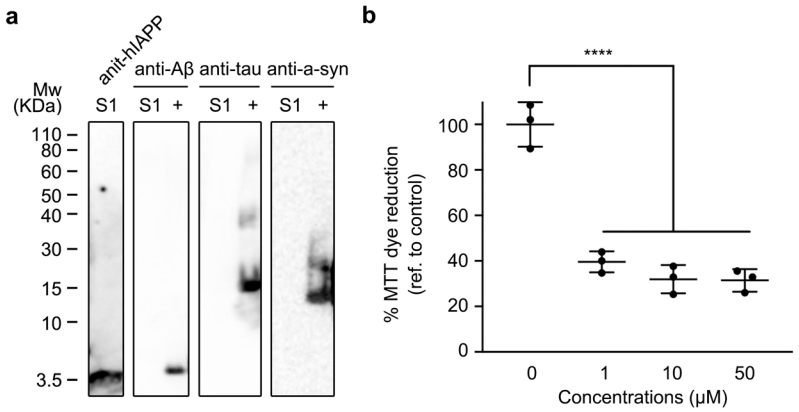

Extended Data Fig. 9 | Western blot of S1 fraction of fibril extraction and MTT assays of seeded hIAPP fibrils. a, Western blot of S1 fraction (originally characterized in Fig. S1b) probed by antibodies that target hIAPP, amyloid-β, tau (K18), and α-synuclein. The only antibody to recognize and label the S1 fraction is anti-hIAPP, suggesting that the S1 fraction consists primarily of hIAPP. Moreover, the molecular weight of the band corresponds to full-length hIAPP. When probed with amyloid-β, tau, and α-synuclein antibodies, bands appear only in positive control lanes (labeled as "+", see Methods for detail). **b**, Rin5F cells were treated with different concentrations of patient-fibril-seeded hIAPP fibrils, and significantly less MTT dye reduction was observed compared to cells without adding fibrils (****$p<0.0001$ using one-way ANOVA test, data are shown as mean ± s.d., n=3 independent experiments).

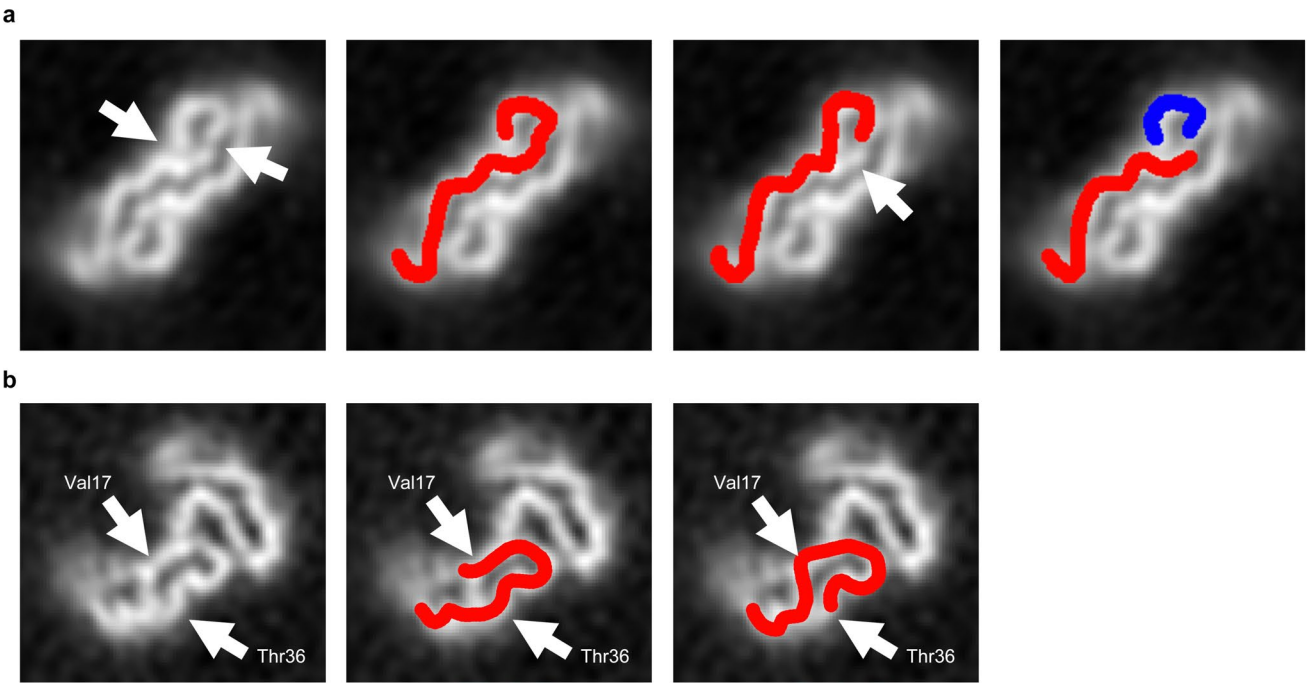

Extended Data Fig. 10 | Main chain tracing of TW2 and TW4. Low resolution 3D reconstructions of TW2 (**a**) and TW4 (**b**) displayed to illustrate the main chain tracing.

nature research

Corresponding author(s): David S. Eisenberg

Last updated by author(s): Jul 14, 2021

Reporting Summary

Nature Research wishes to improve the reproducibility of the work that we publish. This form provides structure for consistency and transparency in reporting. For further information on Nature Research policies, see Authors & Referees and the Editorial Policy Checklist.

Statistics

For all statistical analyses, confirm that the following items are present in the figure legend, table legend, main text, or Methods section.

n/a	Confirmed	
☐	☒	The exact sample size (*n*) for each experimental group/condition, given as a discrete number and unit of measurement
☐	☒	A statement on whether measurements were taken from distinct samples or whether the same sample was measured repeatedly
☐	☒	The statistical test(s) used AND whether they are one- or two-sided *Only common tests should be described solely by name; describe more complex techniques in the Methods section.*
☒	☐	A description of all covariates tested
☒	☐	A description of any assumptions or corrections, such as tests of normality and adjustment for multiple comparisons
☐	☒	A full description of the statistical parameters including central tendency (e.g. means) or other basic estimates (e.g. regression coefficient) AND variation (e.g. standard deviation) or associated estimates of uncertainty (e.g. confidence intervals)
☐	☒	For null hypothesis testing, the test statistic (e.g. *F*, *t*, *r*) with confidence intervals, effect sizes, degrees of freedom and *P* value noted *Give P values as exact values whenever suitable.*
☒	☐	For Bayesian analysis, information on the choice of priors and Markov chain Monte Carlo settings
☒	☐	For hierarchical and complex designs, identification of the appropriate level for tests and full reporting of outcomes
☒	☐	Estimates of effect sizes (e.g. Cohen's *d*, Pearson's *r*), indicating how they were calculated

Our web collection on statistics for biologists contains articles on many of the points above.

Software and code

Policy information about availability of computer code

Data collection	Automated Cryo-EM data collection was driven by SerialEM (version 3.8)
Data analysis	Anisotropic magnification distortion was estimated by software mag_distortion_estimate (version 0.0.0). CTF estimation was performed using CTFFIND (version 4.1.8). Beam-induced motion was corrected by Unblur (version 1.0.0). Particle picking was performed using EMAN2 (version 2.2) e2helixboxer.py and CrYOLO (version 1.7). Classification, helical reconstruction, and 3D refinement were performed in RELION (version 2.1.0). Refined maps were sharpened using phenix.auto_sharpen (version 1.13-2998). Atomic models were built in COOT (version 0.8.9.1). Model refinement was performed with phenix.real_space_refine (version 1.13-2998). Structures were presented using PyMOL (version 2.2.0). ThT curves were generated using GraphPad Prism (version 7.0c). Energetic calculations were performed using custom written software, and the code is available at MBI website (URL: https://people.mbi.ucla.edu/sawaya/amyloidatlas/accessiblesurfacearea_v07.2d.f)

For manuscripts utilizing custom algorithms or software that are central to the research but not yet described in published literature, software must be made available to editors/reviewers. We strongly encourage code deposition in a community repository (e.g. GitHub). See the Nature Research guidelines for submitting code & software for further information.

Data

Policy information about availability of data

All manuscripts must include a data availability statement. This statement should provide the following information, where applicable:

- Accession codes, unique identifiers, or web links for publicly available datasets
- A list of figures that have associated raw data
- A description of any restrictions on data availability

Structural data have been deposited into the Worldwide Protein Data Bank (wwPDB) and the Electron Microscopy Data Bank (EMDB) with accession codes: PDB 7M61, EMD-23686 (TW1); PDB 7M62, EMD-23687 (TW2); PDB 7M64, EMD-23688 (TW3); PDB 7M65, EMD-23689 (TW4). PDB accession codes for previously

reported coordinates used for structural analysis in this study are: 6Y1A, 6ZRR, 6ZRQ, 6ZRF, 6VW2 for hIAPP fibrils and 6OIZ, 2M4J, 2MVX, 5KK3, 5OQV, 2NAO, 2MXU, 2BEG, 2LMN, 2MPZ, 6SHS for Aβ fibrils. All data is available in the manuscript or the supplementary materials.

Field-specific reporting

Please select the one below that is the best fit for your research. If you are not sure, read the appropriate sections before making your selection.

☒ Life sciences ☐ Behavioural & social sciences ☐ Ecological, evolutionary & environmental sciences

For a reference copy of the document with all sections, see nature.com/documents/nr-reporting-summary-flat.pdf

Life sciences study design

All studies must disclose on these points even when the disclosure is negative.

Sample size	Sample sizes for ThT assays and cytotoxicity assays were 3 and are generally considered as sufficient for plate-reader based experiments. The same sample sizes were also used in previous studies performed by our group (e.g. Cao, Q., Boyer, D. R., Sawaya, M. R., Ge, P. & Eisenberg, D. S. Cryo-EM structure and inhibitor design of human IAPP (amylin) fibrils. Nat. Struct. Mol. Biol. (2020) doi:10.1038/s41594-020-0435-3.) and others (e.g. Paul, A., Kalita, S., Kalita, S., Sukumar, P. & Mandal, B. Disaggregation of Amylin Aggregate by Novel Conformationally Restricted Aminobenzoic Acid containing α/β and α/γ Hybrid Peptidomimetics. Sci. Rep. 7, 40095 (2017)). For cytotoxicity assays, these sample size provide sufficient statistical significance during one-way ANOVA test (P value < 0.0001). Sample size for fibril extraction, EM observation, and structure determination was 1, because of the difficulty in acquiring patient samples. We note our study may not be able to address whether the structures we reported here can represent other type II diabetes patients because of the limited sample size, and we have discussed this limitation in the manuscript.
Data exclusions	No data were excluded from the results.
Replication	All attempts at replication were successful. For ThT assays, Western Blot and cytotoxicity assays, experiments were performed at least three times independently. For Congo red staining and EM, replication with the same sample was not applied.
Randomization	Randomization is not relevant to our study. No research animal, human research participants or clinical studies are involved in our study. For each ThT assay, Western Blot and cytotoxicity assay, samples were loaded to a single 96-well plate or membrane, treated equally, and the results were recorded by the automatic plate reader or Western Blot imaging system. So the results should be objective and therefore no randomization is required.
Blinding	Blinding was not relevant to our study. No subjective analysis were required as we described in the randomization above.

Reporting for specific materials, systems and methods

We require information from authors about some types of materials, experimental systems and methods used in many studies. Here, indicate whether each material, system or method listed is relevant to your study. If you are not sure if a list item applies to your research, read the appropriate section before selecting a response.

Materials & experimental systems

n/a	Involved in the study
☐	☒ Antibodies
☐	☒ Eukaryotic cell lines
☒	☐ Palaeontology
☒	☐ Animals and other organisms
☒	☐ Human research participants
☒	☐ Clinical data

Methods

n/a	Involved in the study
☒	☐ ChIP-seq
☒	☐ Flow cytometry
☒	☐ MRI-based neuroimaging

Antibodies

Antibodies used	i) Amylin Polyclonal Antibody (also referred as anti-hIAPP antibody in the manuscript), Invitrogen, Lot no. UH2833361, catalog no. PA5-98309; ii) Anti-amyloid fibrils OC antibody, Millipore, Lot no. 2345063, catalog no. AB2286; iii) Anti-Rabbit IgG, Sigma, Lot no. 023M4757, catalog no. A0545; iv) Anti-α-synuclein antibody MJFR-14-6-4-2, Abcam, Lot no. GR3222269-10, catalog no. ab138501; v) Anti-Aβ antibody 6E10, Biolegend, Lot no. B261546, catalog no. 803003; vi) Anti-tau, Agilent Dako, Lot no. 20024929, catalog no. A002401-2; vii) Anti-Rabbit IgG, Invitrogen, Lot no. 2116291, catalog no. A27036; viii) Anti-Goat IgG, Abcam, Lot no. GR3271082-2, catalog no. ab205719.
Validation	i) Species reactivity: human, mouse; host/isotype: rabbit/IgG; validation/application: western blot analysis and immunohistochemical analysis applied by Thermo Fisher. ii) Species reactivity: human; host: rabbit; validation: evaluated by Dot Blot of amyloid fibrils by Millipore; application: immunoprecipitaton, immunocytochemistry, immunohistochemistry, ELISA, western blotting, dot blot. iv) Species reactivity: human, rat, mouse; host: rabbit; validation: Dot Blot: recombinant alpha-synuclein filament untreated and treated with 70% formic acid; recombinant alpha-synuclein monomer; application: Dot blot,

ICC/IF, IHC-P. v) Species reactivity: human; host: mouse; validation: Herzig M, et al. 2004. Nat. Neuro. 7(9):954-959; Kumar R, et al. 2016. Brain. 139:174-92; application: WB, ELISA, IHC-F, EM, ICC. vi) Species reactivity: human; host: rabbit; validation:Biernat J, Wu Y-Z, Timm T, Zheng-Fischhöfer Q, Mandelkow E, Meijer L, et al. Mol Biol Cell 2002;13:4013-28; application: immunocytochemistry, immunoprecipitation.

Eukaryotic cell lines

Policy information about cell lines

Cell line source(s)	Rin5F cells purchased from ATCC (Lot no. 61465080)
Authentication	Cell line used was not authenticated by us
Mycoplasma contamination	Mycoplasma contamination has been tested by ATCC with Hoechst DNA stain method and agar culture method and the results were negative.
Commonly misidentified lines (See ICLAC register)	No commonly misidentified cell lines were used